Science of the Total Environment 847 (2022) 157656

Contents lists available at ScienceDirect

Science of the Total Environment

journal homepage: www.elsevier.com/locate/scitotenv

Shift in the migration trajectory of the green biomass loss barycenter in Central Asia

Feifei Han [a], Hongbo Ling [b,*], Junjie Yan [c], Mingjiang Deng [d], Xiaoya Deng [e], Yanming Gong [f], Wenqi Wang [b,g]

[a] College of Water Sciences, Beijing Normal University, Beijing 100875, China
[b] State Key Laboratory of Desert and Oasis Ecology, Xinjiang Institute of Ecology and Geography, Chinese Academy of Sciences (CAS), Urumqi 830011, China
[c] Institute of Resources and Ecology, Yili Normal University, Yining 835000, China
[d] Engineering Research Center of Water Resources and Ecological Water Conservancy in Cold and Arid Area of Xinjiang, Urumqi 830011, China
[e] State Key Laboratory of Simulation and Regulation of Water Cycle in River Basin, Department of Water Resources, China Institute of Water Resources and Hydropower Research, Beijing 100038, China
[f] CAS Key Laboratory of Biogeography and Bioresources in Arid Land, Xinjiang Institute of Ecology and Geography, Urumqi 830011, China
[g] University of Chinese Academy of Sciences, Beijing 100049, China

HIGHLIGHTS

- Quantify vegetation vulnerability under historical and future drought scenarios.
- Quantification revealed the mechanism of drought-induced vegetation degradation.
- Migration laws of the vegetation loss barycenter in Central Asia was revealed.
- Diagnosing the effectiveness of the China's proactive strategy to cope with global climate change.

GRAPHICAL ABSTRACT

Migration trajectory of vegetation loss barycenter in CA. 'Historical' refers to the vegetation loss barycenter in historical periods, 'SSP126-NFP' refers to the vegetation loss barycenter in the NFP under the SSP126 scenario; 'SSP126-FFP' refers to the vegetation loss barycenter in the FFP under the SSP126 scenario; 'SSP245-NFP' refers to the vegetation loss barycenter in the NFP under the SSP245 scenario; 'SSP245-FFP' refers to the vegetation loss barycenter in the FFP under the SSP245 scenario; 'SSP585-NFP' refers to the vegetation loss barycenter in the NFP under the SSP585 scenario; 'SSP585-FFP' refers to the vegetation loss barycenter in the FFP under the SSP585 scenario.

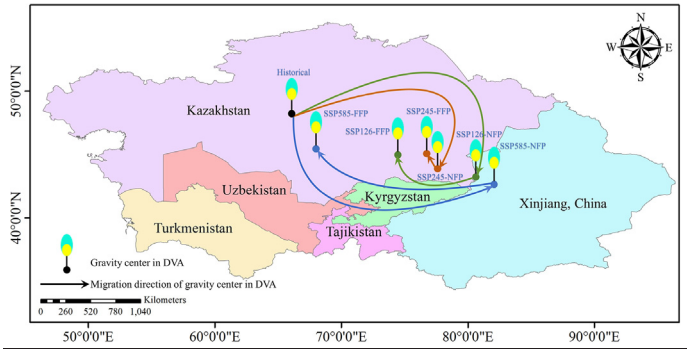

ARTICLE INFO

Editor: Martin Drews

Keywords:
Green biomass loss
Drought stress
Central Asia
Global climate change

ABSTRACT

Revealing the vegetation response law under drought stress has become a hot issue in global climate change research. Against the background of human beings actively responding to climate change, quantitatively revealing the change and migration laws of green biomass loss (GBL) caused by drought in historical and future periods is insufficient. In this regard, we innovatively constructed a joint kNDVI-SPEI (kernel normalized difference vegetation index and standardized precipitation evapotranspiration index) distribution based on copula theory to accurately capture GBL dynamic under various drought scenarios unlike previous studies conducted in a deterministic way. Taking the drought-sensitive and ecologically vulnerable Central Asia (CA) as a typical region, we verified that an average 94.4 % of region showed greater vegetation vulnerability in times of water shortage from May to October, which exhibited the greatest probability of GBL under different drought scenarios, mainly in Kazakhstan and Uzbekistan. Significantly intensified drought due to high emissions will cause an 18.16 percentage-point increase in GBL probability in the far future

* Corresponding author.
E-mail address: linghb@ms.xjb.ac.cn (H. Ling).

http://dx.doi.org/10.1016/j.scitotenv.2022.157656
Received 11 May 2022; Received in revised form 19 July 2022; Accepted 23 July 2022
Available online 27 July 2022

(FFP, 2061–2100) compared to the near future (NFP, 2019–2060), which is much higher than in the lower-emission (0.38 %) and moderate-emission scenarios (9.82 %). In the NFP, the GBL barycenter will shift from Kazakhstan to Xinjiang, China; in the FFP, it will shift back to Kazakhstan due to the measures taken by the Chinese government to conserve energy and reduce emissions. Results illustrate that against the background of worsening drought, active climate change coping strategies can reverse the migration trajectory of the GBL barycenter caused by drought, which provides a new idea for vegetation protection research in response to global climate change.

1. Introduction

Drought is a severe natural disaster that occurs when water availability is significantly below normal for a long time (Wilhite et al., 2007). The duration, frequency, and intensity of drought are increasing due to increased evapotranspiration from global climate change and decreased regional precipitation (Christian et al., 2021; Sheffield et al., 2012). Frequent and severe droughts often have a far-reaching negative impact on ecosystem health (Gampe et al., 2021), agricultural production (Abdelmalek and Nouiri, 2020), water resources (Pedro-Monzonís et al., 2015), and the environment, which is more significant in ecologically fragile arid areas (Li et al., 2020). To slow down the expansion of drought, many countries have taken a series of measures such as returning farmland to forest, restoring water conservation measures, and optimizing the layout of agricultural production (Bryan et al., 2018; Pedro-Monzonís et al., 2015). In various natural and human systems sensitive to water variability, terrestrial ecosystems have distinct and complex interactions with drought (Martínez-Vilalta and Lloret, 2016). Drought severely limits the main physiological processes of vegetation (Vicente-Serrano et al., 2013) and carbon dioxide absorption (Ma et al., 2012), and persistent water shortage adversely affects vegetation function, leading to slow growth, decreased biomass, and death and being one of the main drivers of reduced aboveground net primary productivity (Drew, 1979; Sun et al., 2018). Due to the long duration of drought, the drought will have a certain impact on the entire terrestrial vegetation ecosystem in the long run (Ding et al., 2020; Ji and Peters, 2003). Worse still, with terrestrial vegetation as the main carbon pool on earth, the intensity of terrestrial carbon sinks may be shifting from an increasing trend to a decreasing one due to the effects of drought on vegetation growth (Ma et al., 2012). Therefore, quantitatively understanding the laws of terrestrial vegetation response to drought and identifying drought-vulnerable areas are of great significance for ecosystem restoration and protection in arid areas.

Assessing the impact of drought on terrestrial vegetation is strongly challenged by difficulties in drought quantification and the integrated response of vegetation activity to various climate and anthropogenic factors. Compared with other natural disasters, drought occurs and develops slowly and in a complex manner (Wilhite et al., 2007); previous quantitative drought studies have mainly relied on various drought indicators, physical models, and water balance simulations (Bachmair et al., 2016; Pedro-Monzonís et al., 2015). Because drought indicators are a convenient way to quantify the duration, intensity, and impact of droughts, they enable different users to communicate drought information more effectively and are often used to describe long-term changes in drought events (Zargar et al., 2011). The standardized precipitation evapotranspiration index (SPEI), which is based on precipitation and potential evapotranspiration (PET), can reflect the water deficit in a changing environment and has multi-scalar characteristics (Beguería et al., 2014), making it conducive to the unified evaluation of vegetation response to short-, medium-, and long-term drought. Hence, SPEI was used to characterize drought in this study. Previous studies have used vegetation indices such as the enhanced vegetation index (EVI), the near-infrared reflectance (NIRv), and the normalized difference vegetation index (NDVI) to monitor vegetation dynamics (Camps-Valls et al., 2021; Peng et al., 2020), but these indices have certain limitations. Compared with other vegetation indices, NDVI can partially eliminate the effects of cloud cover and terrain changes after post-processing, and is widely used by many researchers (Camps-Valls et al., 2021; Xu et al., 2021). However, the relationship between NDVI and vegetation biomass is nonlinear, often reaching saturation before the maximum biomass is observed (Pinzon and Tucker, 2014). Therefore, this study chose the kernel NDVI (kNDVI), which was proposed by a recent study to monitor vegetation changes (Camps-Valls et al., 2021). The index is based on the kernel method theory in machine learning, which eliminates the problem of linear assumptions in the NDVI calculations and maximizes the use of satellite spectral information (Camps-Valls et al., 2021; Hofmann et al., 2008). Existing studies have shown that kNDVI performs well in monitoring vegetation dynamics in arid areas, providing the possibility of assessing vegetation vulnerability in the study area (Wang et al., 2021; Wang et al., 2022). To quantify vegetation vulnerability, this study defines GBL as the probability of damage to terrestrial vegetation ecosystems when drought occurs (Fang et al., 2019a; Fang et al., 2019b). At the same time, in order to conduct a more comprehensive drought assessment, this study uses kNDVI at 0.4, 0.3, 0.2, and 0.1 quantiles to characterize the different states of terrestrial vegetation ecosystems. When kNDVI is less than the smaller quantile value, we believe that the local terrestrial vegetation ecosystem has suffered serious damage, that is, serious GBL (Newbold et al., 2015). The sensitivity of terrestrial vegetation to water changes as well as its response time can be quantitatively assessed by correlating kNDVI and SPEI at different time scales. The maximum Pearson correlation coefficient between kNDVI and SPEI at different scales was used to measure the sensitivity of vegetation to drought, and the SPEI time scale corresponding to the maximum correlation coefficient was taken to be the vegetation response time (Fang et al., 2019b). In this paper, we define drought resistance as the maintenance of photosynthetically active tissues ensuring plant growth during drought events (Verslues et al., 2006). Resilience is the aptitude of a plant or a community to recover its physiological functions and productivity after drought to levels comparable to those measured before the stress (Dalal et al., 2019). The vegetation response time refers to the lag time between the onset of water deficit and the obvious impact on vegetation (Fang et al., 2019b). It emphasizes that the effects of drought on vegetation are not instantaneous, but the cumulative result of water deficits over a period of time. Therefore, vegetation response time can be used to reflect the drought resistance of vegetation (Fang and Xiong, 2015), and the longer the response time, the stronger its ability to resist long-term water shortage. In general, vegetation in arid areas has mechanisms that can quickly adapt to changes in water resources and can respond quickly when drought occurs (Vicente-Serrano et al., 2013). Vegetation in wet areas also responds to drought for a short period of time, but in this case, vegetation is often degraded from poor adaptability to water shortages. In contrast, although vegetation in semi-arid and sub-humid lands is resistant to water scarcity, it does not respond as quickly to drought as vegetation in arid or humid lands (Bai et al., 2019) and therefore has a longer response time. Understanding vegetation response times in different types of regions can improve our understanding of vegetation vulnerability in the context of climate change.

From the perspective of decision-makers, merely analyzing the correlation between kNDVI and SPEI is not enough to understand the GBL situation sufficiently well to take drought preparedness measures. At the same time, as climate change and human activity constantly increase, future droughts may become more intense (Dai, 2013; Sherwood and Fu, 2014), leading to enhanced vegetation vulnerability and expansion of drought-vulnerable areas. Therefore, future change trends in drought and the migration law of the GBL barycenter are the scientific issues of concern in

this study. In addition, to alleviate deterioration of the ecological environment caused by global climate change, the international community has adopted measures such as energy conservation and emissions reduction, development of new energy sources, and strengthening of international cooperation. Studies have shown that if the commitments made by governments around the world to deal with climate change can be achieved, the 2 °C temperature rise target set by the Paris Agreement is highly likely to be achieved (Meinshausen et al., 2022; Ou et al., 2021a; Ou et al., 2021b). This shows the effectiveness of the measures taken by governments in energy conservation, emission reduction and mitigation of global warming (Borrelli et al., 2020). Therefore, the authors have hypothesized that positive climate change response strategies may shift the migration trajectory of the GBL barycenter caused by drought.

To solve these scientific problems and test this hypothesis, the copula function (Li, 2000), a multidimensional joint distribution function with a uniform distribution in the domain [0,1], is introduced. Unlike previous modelling methods, it can construct a multi-dimensional joint distribution with two parts, the marginal distribution and the correlation structure, and then simulate the dependency structure of any correlated variable (Salvadori and De Michele, 2004). Due to the flexible and diverse forms of the copula function, any two or more variables with correlation can theoretically have their dependence structure characterized with the copula function (Genest et al., 2009; Li, 2000). In recent years, the copula function has been widely used in flood analysis, rainfall forecasting, drought characteristic analysis, and hydrological stochastic simulation (Yang et al., 2018). Based on historical observational data, this study calculated GBL probability under a given drought scenario by constructing a vegetation-drought relationship model combined with the concept of conditional probability and then identifying drought-vulnerable areas under the current situation. For future periods, drought-vulnerable areas can be identified directly using Earth climate system models. In terms of predicting future climate change, the newly released Coupled Model Intercomparison Project Phase 6 (CMIP6) uses a more reasonable shared socioeconomic pathway (SSP) that considers various future changes in greenhouse gases with other radiative forcing and socioeconomic development (O'Neill et al., 2016). Compared with CMIP5, it is more reliable and stable (Li et al., 2021; Wu et al., 2019). Studies have shown that CMIP6 has achieved great improvements in many drought-related studies and is more in line with the latest reference estimates of global energy balances (Li et al., 2021). Therefore, this study used the output of the CMIP6 model under high-, medium-, and low-forcing scenarios to study the trend of future drought changes and took future drought as a conditional input to the vegetation-drought relationship model to evaluate changes in vegetation vulnerability in the short term (2019–2060) and the long term (2061–2100) under different future climate change contexts.

This study used a bivariate probabilistic framework based on copula theory, which primarily relies on recognizing the response time of vegetation dynamics to water variability on a monthly time scale using Pearson correlation analysis, describing the dependence structure of vegetation status and drought conditions using the copula function, and estimating the probabilities of GBL under multiple drought scenarios. Afterwards, the impact of drought on terrestrial vegetation was quantified, drought-vulnerable areas in historical and future periods were identified, and the migration law of the GBL barycenter was revealed. The research results are of great significance for revealing the response laws of terrestrial vegetation to drought, promoting ecological protection and restoration, and helping decision-makers to formulate strategies in a timely manner to deal with GBL caused by global climate change.

2. Materials and methods

2.1. Study area

Central Asia (CA) is one of the most ecologically fragile regions in the world with the most serious ecological degradation, which seriously restricts the economic and social development of the region and has drawn wide attention from the international community (Bai et al., 2019; Chen et al., 2019). CA covers an area of about 5.66 × 106 km2, including Kazakhstan, Tajikistan, Kyrgyzstan, Uzbekistan, Turkmenistan, and the Xinjiang Uyghur Autonomous Region in northwestern China (Fig. 1a). Located in the hinterland of Eurasia, CA has a typical continental climate, transitioning from semi-arid to arid regions from north to south, with hot and dry summers and cold and wet winters (Fitzsimmons et al., 2020). The average annual precipitation in the region is <150 mm, decreasing gradually from west to east, with more mountains than basins and plains, and an extremely uneven spatial distribution (Wang et al., 2018). In terms of topography, the overall topography is high in the southeast and low in the northwest and is roughly divided into three zones: high mountainous areas in the southeast, plain areas in the west, and low mountainous hilly areas in the north and center (Fitzsimmons et al., 2020). The study area contains river and lake systems such as the Aral Sea, Lake Balkhash, Amu Darya, Syr Darya, and Tarim Darya (Huang et al., 2021). These are mostly inland rivers, and their water mostly disappears into the desert, except when diverted for irrigation. Rangeland Desert area occupy about a quarter of CA (Huang et al., 2021). The principal land use types (Fig. 1b) are rangeland, sparse vegetation, cropland and so on. It can be seen that most of the area is covered by rangeland, dominated by perennial herbs such as various feather grass and Leymus ramosus (Kamp et al., 2016; Nunez et al., 2020). Studies have shown that the regional mean grassland (i.e. rangeland in this study) NPP for CA during 1982–2015 was approximately 152.7 $gCm^{-2}\ yr^{-1}$ and trending upward significantly at a rate of 0.66 $gCm^{-2}\ yr^{-1}$(Chen et al., 2020). In addition, most rangelands in CA are arid and semi-arid, suitable for large-scale livestock production. In the context of global climate change, the frequent occurrence of extreme climate and hydrological events in CA, especially the frequent occurrence of drought events, has led to serious loss of the region's vegetation and severe land desertification (Jiang et al., 2019). At the same time, as the largest arid zone in the Northern Hemisphere, its dryland ecosystems support a considerable proportion of the population and the economy (Guan et al., 2019), and therefore it is important to analyze the impact of drought on vegetation in the region for sustainable development and drought risk management in CA.

2.2. Data source and pre-processing

2.2.1. Standardized precipitation evapotranspiration index (SPEI)

This paper uses drought indicators to quantify droughts. The most widely used drought indicators are SPEI, SPI, and PDSI. PDSI uses precipitation and temperature to estimate soil moisture supply and demand through a two-level model and is often used to characterize the regional extent and severity of various drought events (Tian et al., 2018; Zargar et al., 2011). However, the fixed time scale makes PDSI unsuitable for characterizing hydrologic droughts, and it is unresponsive to developing droughts (Tian et al., 2018). SPI and SPEI, which are based on long-term meteorological observations, overcome this drawback and can be calculated for various time scales (Stagge et al., 2015). SPI explains abnormal water deficits based on precipitation anomalies, emphasizing precipitation as the main driver of drought. However, the profound influence of temperature in drought development has been observed in typical drought events occurring in Europe, East Asia, and the western United States (Niinemets and Valladares, 2006). Studies have shown that drought is not only influenced by precipitation, but is also closely related to evapotranspiration (Beguería et al., 2014). The increased evapotranspiration demand caused by increasing temperatures can drive the water balance closer and closer to lower values, thus exacerbating water stress. Realizing the potential drawbacks of SPI in the context of global warming, Vicente Serrano et al. developed SPEI using the difference between precipitation and evapotranspiration and used a log-logistic probability distribution function with three parameters to describe its variability (Vicente-Serrano et al., 2010a).

The SPEI data used in this study were obtained from the Web repository of the Spanish National Research Council (Vicente-Serrano et al., 2010b) (CSIC; available online at http://sac.csic.es/spei/index.html). This dataset

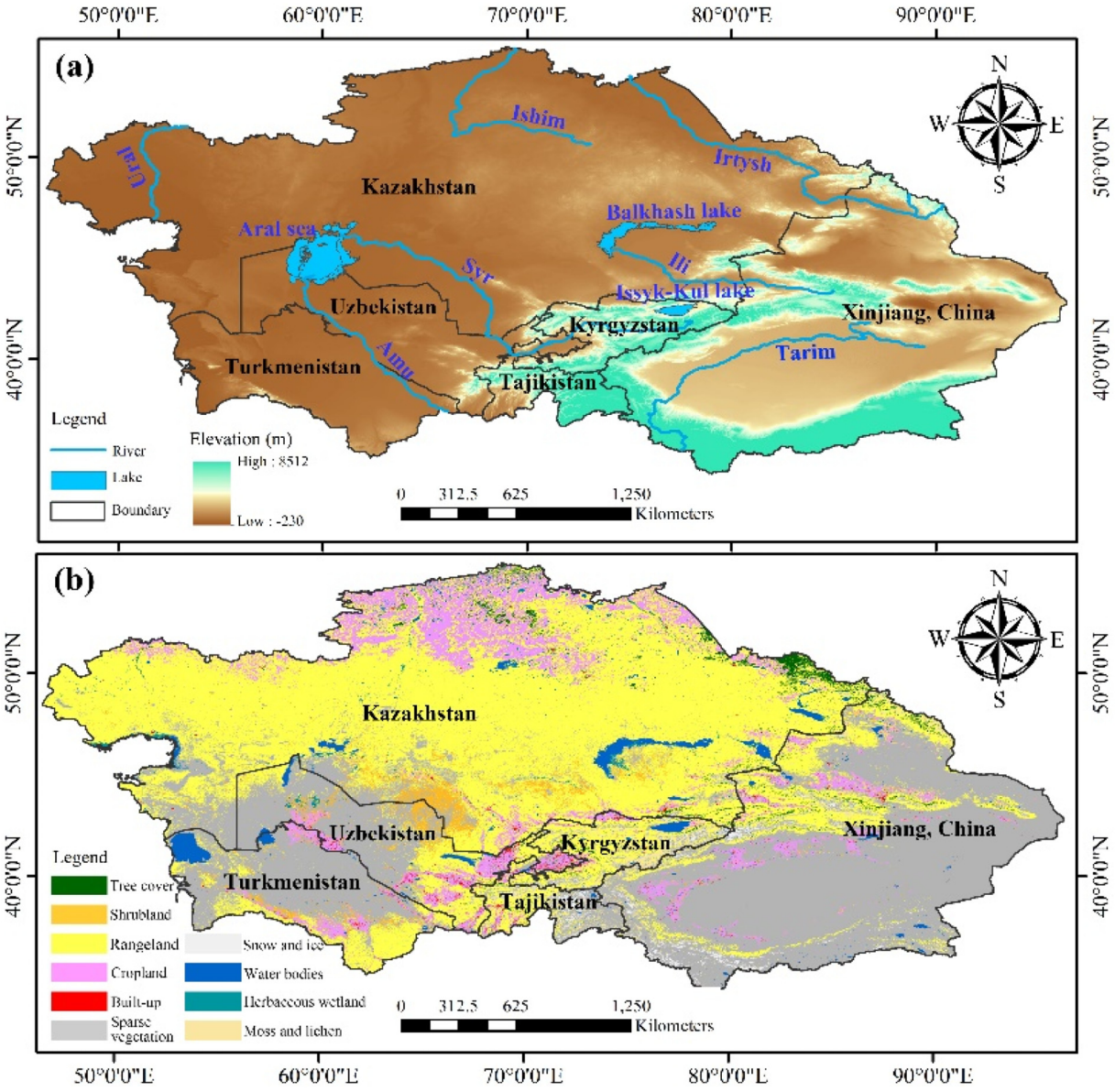

Fig. 1. Schematic map of study area. (a) Map of administration units, cities, digital elevation model, rivers, and main lakes in CA. (b) Distribution of land cover type in CA.

provides long-term reliable information on drought conditions on a global scale, with a SPEI time scale of 1–48 months, and the latest version of SPEIbase, v2.6, covers the period from 1901 to 2018. The new dataset improves the spatial resolution of the unique global drought dataset on global scale. And due to the multi-scale character of SPEI, it is able to identify various drought types (Beguería et al., 2014; Vicente-Serrano et al., 2010b). In addition, the dataset has a 0.5-degree spatial resolution and a monthly time resolution, which meet the needs of this study. Therefore, the SPEI data were extracted by a program based on the Python language on a monthly scale of 1–24 months from 1982 to 2018.

2.2.2. Climate model datasets

Climate scenarios are the basis for climate modelling, and climate projections based on different scenarios are one of the core elements of successive Intergovernmental Panel on Climate Change (IPCC) scientific assessments, the results of which show the climate impacts and socioeconomic risks associated with different policy choices and are an important scientific basis for government decision-making (Wigley and Raper, 1992). The IPCC proposed five shared socioeconomic pathways (SSPs) in 2010, which consider population change, economic development, technological progress, and resource use, to better describe the relationship between climate change and socioeconomic development pathways (Riahi et al., 2017). SSPs are now being used as important inputs to the latest climate models and have enabled significant progress in assessing future temperature and precipitation in various locations (Li et al., 2021). This study uses the output data of the medium-resolution climate system model published by the Beijing Climate Center (BCC-CSM2-MR), which uses improved parameterization results and physical parameterization preference results (Wu et al., 2019). Compared to other CMIP5 atmospheric model versions (BCC-AGCM2.1 and BCC-AGCM3-MR), the model has improved atmospheric radiation, deep convective processes, and gravity wave schemes that can make it more adaptable to the climate distribution (Lu et al., 2021; Wu et al., 2019). Based on this, climate change scenarios from the BCC-CSM2-MR climate model with SSP126 (low radiative forcing), SSP245 (medium radiative forcing), and SSP585 (high radiative forcing) were used here with data for the three shared socioeconomic pathways, including monthly precipitation (pr) and monthly air temperature (tas) data from 2019 to 2100 with a spatial resolution of 1.125°, securing the first variant label "r1i1p1f1" ("r1i1p1f1" refers to the experiment label, where r denotes the realization index (set membership index), i

denotes the initialization index, p denotes the physics index, and f denotes the forcing index). Based on the temperature and precipitation data, monthly SPEI values were calculated on a 12-month scale from 2019 to 2100 under three future climate change scenarios, after which future drought trends could be detected using the Sen'slope and Mann-Kendall tests, and the basic principles and detailed calculations could refer to Gocic et al. (Gocic and Trajkovic, 2013). To match the spatial resolution of the data, the calculated SPEI was resampled to 0.5° spatial resolution using the nearest-neighbor interpolation method.

2.2.3. A unified vegetation index for better monitoring vegetation dynamics

Among various remote-sensing products, NDVI is widely used to monitor the status of terrestrial vegetation and assess the impact of climate change on vegetation status (Camps-Valls et al., 2021; Xu et al., 2021). NDVI is theoretically in the interval [−1,1], and it is usually considered to indicate the presence or absence of vegetation when its value is greater than −0.1 or <0.1(Tucker et al., 2005). Therefore, the raster with NDVI <0.1 was not considered in this study for subsequent calculations. Compared with other ground-based vegetation indices, NDVI is more attractive to researchers because of its global area coverage and high spatiotemporal resolution. However, this index also has some limitations, NDVI uses nonlinear stretching to enhance the contrast of NIR and R reflectance and is less sensitive to high-vegetation-density areas (Pinzon and Tucker, 2014; Tucker et al., 2005). Therefore, this study introduced the kNDVI to monitor vegetation dynamics. The construction method of this index maximizes the use of spectral information, solves a long-standing problem in Earth biosphere satellite observation, and is an accurate proxy for GPP in closer monitoring of vegetation photosynthetic activity (Camps-Valls et al., 2021). In addition, kNDVI enables more accurate measurements of terrestrial carbon source/sink dynamics and the potential for stabilizing atmospheric CO2 and mitigating global climate change (Camps-Valls et al., 2021).

kNDVI is based on the kernel method theory of machine learning, which has been widely used to derive nonlinear algorithms from linear ones (Camps-Valls et al., 2021; Hofmann et al., 2008). Kernel methods can be applied to any vegetation index. The method is used here to generalize NDVI, mainly because of the long history and wide utility of this index, most notably to perform global and long-term studies. To obtain kNDVI, NDVI was mapped in Hilbert spaces, and kernelization was done using the radial basis function (RBF). The formula for calculating kNDVI is:

$$kNDVI = \frac{k(n,n) - k(n,r)}{k(n,n) + k(n,r)} \tag{1}$$

where n, r refer to the remote-sensing reflectance in the NIR and red channels respectively and the kernel function k measures the similarity between the two bands. The kernel function k is calculated using the RBF kernel as follows:

$$k(a,b) = \exp\left(-\frac{(a-b)^2}{2\sigma^2}\right) \tag{2}$$

where a, b are the two bands and the σ parameter determines the notion of distance between the NIR and red bands. A reasonable choice is to take the average value $\sigma = 0.5(NIR + red)$ (for mathematical and ecophysiological justifications please refer to Camps-Valls et al. (Camps-Valls et al., 2021)), which leads to a simplified operational index version expressed as follows:

$$kNDVI = \tanh\left(NDVI^2\right) \tag{3}$$

In this study, Eq. (3) was used to find kNDVI directly through NDVI, using NDVI data from the Global Inventory Monitoring and Mapping System (GIMMS) group (https://climatedataguide.ucar.edu/climate-data/ndvi-normalized-difference-vegetation-index-3rd-generation-nasagfsc-gimms). The GIMMS-NDVI dataset with a spatial resolution of 8 km × 8 km and a temporal resolution of 15 days was produced from imagery provided by the Advanced Very High-Resolution Radiometer (AVHRR) onboard a group of National Oceanic and Atmospheric Administration meteorological satellites (Pinzon and Tucker, 2014). Bias correlation was performed to alleviate the adverse influence of volcanic eruptions, sensor drift, and atmospheric contamination. Data quality assessment at global scale indicates that the long-term vegetation trends derived from the GIMMS-NDVI are considered reliable except in Equatorial and Arctic areas (Fensholt and Proud, 2012). To match the temporal and spatial resolution of SPEI, the maximum value synthesis (MVC) method (Pinzon and Tucker, 2014) was used to aggregate GIMMS-NDVI images from every two periods to generate a monthly scale sequence and to upscale the resolution to 0.5° × 0.5° using the nearest-neighbor interpolation method. Because this study covers the time range from 1982 to 2018, the Moderate Resolution Imaging Spectroradiometer (MODIS) NDVI dataset was used to extend the GIMMS-NDVI data; cross validation showed that the correlation coefficient between these two datasets exceeded 0.8(Fang et al., 2019a).

2.3. Data analysis

Unlike previous vulnerability assessments that rely primarily on deterministic approaches such as correlation analysis, this study used a binary probabilistic framework based on copula theory to quantify GBL from a probabilistic perspective across multiple drought contexts in past and future periods and to reveal the migration laws of the GBL barycenter in CA (Schematic diagram of research ideas is shown in Fig. 2).

2.3.1. Determination of vegetation response time to water variability

The SPEI has multi-scale characteristics and can be calculated for different time scales. The SPEI on a monthly basis denotes the standardized precipitation accumulation over the preceding several months (Wang et al., 2011). In this study, month-by-month SPEI series at scales of 1–24 months from 1982 to 2018 were selected and correlated with the kNDVI series of the corresponding period to filter the response time of vegetation to water variability. For the i-th month in a year, Pearson's correlation analysis was performed between the monthly kNDVI and the SPEI series at different time scales:

$$R_j^i = corr\left(kNDVI^i SPEI_j^i\right)\ i = 1, 2, \ldots, 12;\ 1 \le j \le 24 \tag{4}$$

where R_j^i denotes the correlation coefficient between the kNDVI series of the i-th month and the SPEI series of the j-th month, after which the vegetation response time (VRT) was calculated using the following equation

$$VRT^i = \arg \max_{1 \le j \le 24} \left\{R_j^i\right\} \tag{5}$$

The vegetation response time is defined as the time scale that maximizes the kNDVI-SPEI association, where VRT^i denotes the vegetation response time to water variability for the i-th month. Examination of multiple SPEI time scales provides increased knowledge about how vegetation health varies in response to precipitation anomalies and clarifies the time lag between two important variables.

2.3.2. A copula-based method for quantifying GBL probability under multiple drought scenarios

The copula function is an effective way to construct a multidimensional joint distribution model. Unlike other multivariate analysis calculation methods, it can decompose the joint distribution into two parts, the marginal distribution and the correlation structure, and then handle them separately (Salvadori and De Michele, 2004). On the one hand, the joint distribution can be constructed by the copula function for any marginal distribution; on the other hand, the computational results of the original univariate analysis can be used, thus simplifying the complex work of studying the joint distribution into studying the correlation structure between variables. Currently, this method is widely applied in drought assessment and ecological studies (Borgomeo et al., 2015). This study uses a binary probabilistic framework based on copula theory to describe the complex dependence structure between drought and vegetation by calculating the probability of GBL under different drought scenarios. Given the

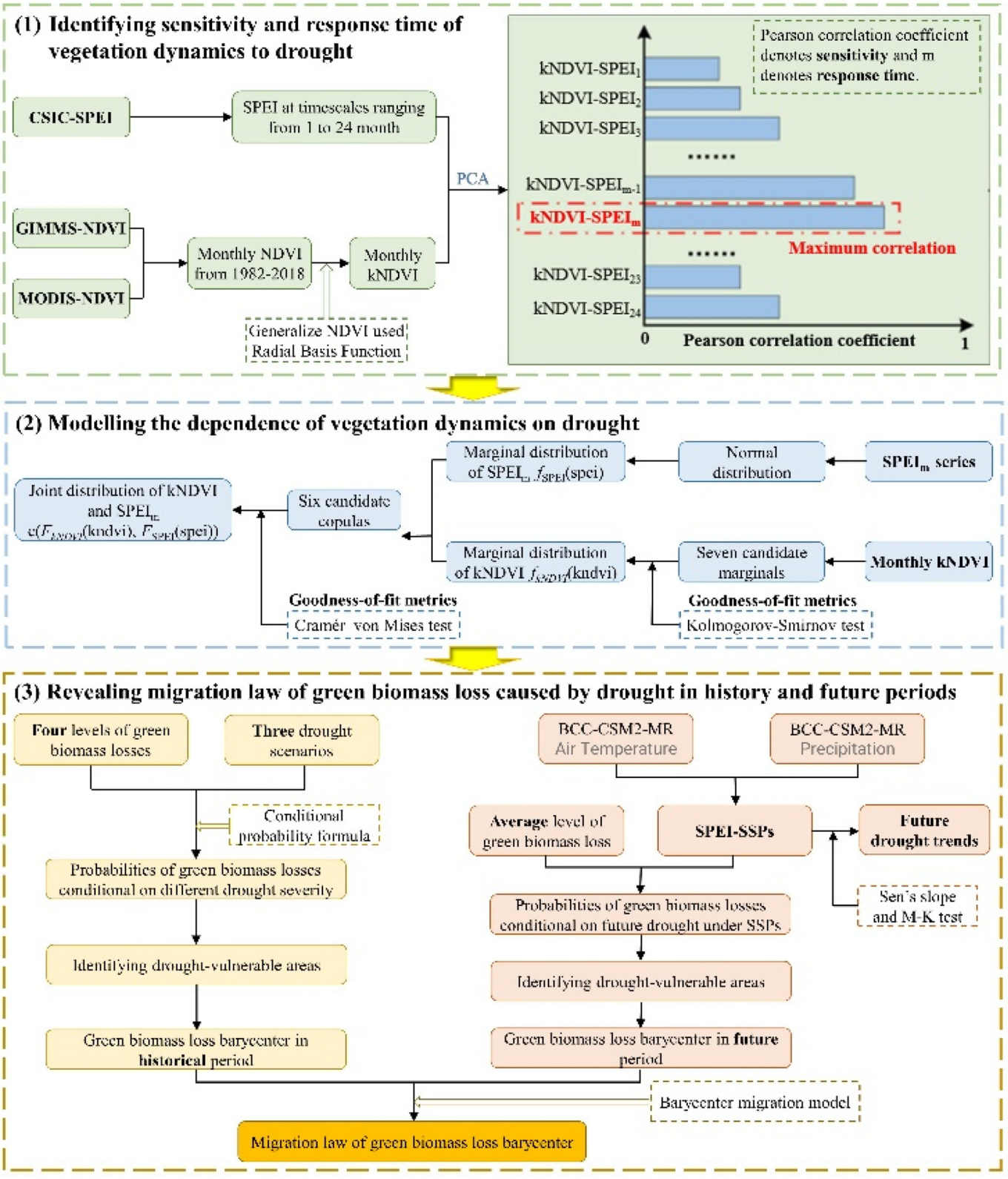

Fig. 2. Schematic diagram of research ideas.

vegetation response time recognized at the x-month scale of the SPEI, the corresponding joint distribution can be expressed as follows

$$F_{SPEI_x,kNDVI}(spei, kndvi) = P(SPEI_x < spei, kNDVI < kndvi) = C(F_1(spei), F_2(kndvi)) \quad (6)$$

where C() denotes the copula function and $F_1(spei)$ and $F_2(kndvi)$ are the edge distributions of the $SPEI_x$ and *kNDVI* sequences respectively. Unlike past methods of constructing joint distributions, which generally directly join the original random variables of interest, the copula function uses its cumulative distribution functions (CDFs) as independent variables. Therefore, the edge distribution functions of the $SPEI_x$ and *kNDVI* sequences

must be fitted separately. In this study, the normal, logistic-normal, logistic, Weibull, GEV, Gumbel, and exponential distributions were fitted to the monthly kNDVI series, among which the optimal marginal was derived according to the Kolmogorov-Smirnov (KS) test. According to the SPEI calculation principle, SPEI is a normalized variable, and the normal distribution was used as its marginal distribution. Next, six commonly used copula functions in the Archimedean and elliptical families were selected to model the dependencies between kNDVI and SPEI, which consisted of the Gaussian, Student's t, Frank, Clayton, Gumbel, and Joe types (for the specific function form and introduction, please refer to Li et al. (Li, 2000)). The maximum likelihood estimation (MLE) method was used to calculate the copula parameters. Finally, a goodness-of-fit test based on Rosenblatt's transform was used to select the copula function with the best performance. This test produced two evaluation metrics with the smallest Cramér-von Mises statistic and the largest *p*-value, which were considered to be optimal inside the candidate copula function. Note that the Joe, Gumbel, and Clayton copulas are limited to interpreting positive correlations, and when negative correlations between kNDVI and SPEI occurred, only the best copula functions were filtered from the Gaussian, Student's t, and Frank copula functions, which are effective for handling both negative and positive SPEI-NDVI correlations. More details about the theoretical justifications and the goodness-of-fit test are available in Salvadori and De Michele (Salvadori and De Michele, 2004) and Genest et al. (Genest et al., 2009).

Beyond understanding the impact of drought on vegetation, ecologists, decision-makers, and crop producers are concerned with the probability of GBL in the event of future droughts, which can be expressed as a conditional probability from a statistical perspective. Therefore, according to the SPEI drought classification table, three drought scenarios were defined: moderate ($-1.5 < \mathrm{SPI} \leq -1$), severe ($-2 < \mathrm{SPI} \leq -1.5$), and extreme ($\mathrm{SPI} \leq -2$). Given multiple drought scenarios, conditional probabilities of kNDVI being lower than specific percentiles (the 40th, 30th, 20th, and 10th percentiles) were derived using the copula-based joint distribution and the conditional distribution formulas. By denoting the observed values of kNDVI at different percentiles as 'kndvi', the expressions in the three drought scenarios become P(kNDVI < kndvi | -1.5 < SPEI ≤ -1), P(kNDVI < kndvi | -2 < SPEI ≤ -1.5), and P(kNDVI < kndvi | SPEI ≤ -2). Each of these, in fact, represents the vegetation response to a class of droughts (denoted by the SPEI varying over a continuous range). And the calculation formula is as follows.

$$P(\mathrm{kNDVI} < \mathrm{kndvi} \mid -1.5 < \mathrm{SPEI} \leq -1) = \frac{P(-1.5 < SPEI \leq -1,\ kNDVI < kndvi)}{P(-1.5 < SPEI \leq -1)} \tag{7}$$

$$P(\mathrm{kNDVI} < \mathrm{kndvi} \mid -2 < \mathrm{SPEI} \leq -1.5) = \frac{P(-2 < SPEI \leq -1.5,\ kNDVI < kndvi)}{P(-2 < SPEI \leq -1.5)} \tag{8}$$

$$P(\mathrm{kNDVI} < \mathrm{kndvi} \mid \mathrm{SPEI} \leq -2) = \frac{P(SPEI \leq -2,\ kNDVI < kndvi)}{P(SPEI \leq -2)} \tag{9}$$

For an upcoming drought, the SPEI can be calculated using the future climate change data output from the climate model, which will be denoted as 'spei0'. The probability of GBL when 'spei0' occurs can be expressed as P (kNDVI < kndvi | SPEI = spei0), and its probability density function (PDF) can be inferred from the Bayesian network and calculated as follows:

$$f_{kNDVI|SPEI_x}(kndvi \mid \mathrm{spei}_0) = c\left[f_{SPEI_X}(\mathrm{spei}_0), f_{kNDVI}(kndvi)\right] \times f_{kNDVI}(kndvi) \tag{10}$$

where c(u,v) denotes the probability density function of the copula function and $f_{SPEI_x}(spei)$ (spei) and $f_{kNDVI}(kndvi)$ (kndvi) denote the probability density functions of SPEI and kNDVI respectively. Once the conditional PDF $f_{kNDVI|SPEI_x}(kndvi \mid \mathrm{spei}_0)$ for a given drought condition has been computed using Eq. (7), the cumulative probability of GBL to a particular threshold can be calculated by the area under the $f_{kNDVI|SPEI_x}(kndvi \mid \mathrm{spei}_0)$ curve for kNDVI < kndvi. Calculating the probabilities of GBL under specific drought conditions can help in further quantitative assessments of the impact of drought on vegetation and the identification of drought-vulnerable areas from a probabilistic perspective.

2.3.3. Identifying the GBL barycenter

The GBL barycenter refers to the fulcrum of the distribution of GBL in a certain area on the space plane at a certain time node to make the moment reach equilibrium (Ahmad, 2017; Hu et al., 2019). Linking all the GBL barycenter at different time nodes can reveal the migration law of the GBL barycenter in this area. The barycenter migration model is an effective method to reflect the spatial evolution of objects and can describe the dynamic migration of the center of gravity of GBL in different periods (Jiang et al., 2020a). It is widely used in many studies of spatial processes and patterns, such as regional population flow, economic changes, soil erosion, and landscape pattern evolution (Hu et al., 2019; Jiang et al., 2020a). In this study, hot spots analysis was first used to identify GBL hot-spots in space, and then the coordinates of the barycenter of the hot-spot areas were calculated. Hot spots analysis can be used to check for statistically significant high and low values in local areas and to display hot- and cold-spot areas using visualization (Reddy et al., 2016). Hot spots analysis often uses the local Getis-Ord G* index, which is calculated as follows:

$$G_i^*(d) = \frac{\sum_j^n W_{ij}(d)X_j}{\sum X_j} \tag{11}$$

Normalization of $G_i^*(d)$ yields

$$Z(G_i^*) = \frac{G_i^* - E(G_i^*)}{\sqrt{Var(G_i^*)}} \tag{12}$$

where X_j denotes the GBL probability value of the j-th raster, $E(G_i^*)$ and $Var(G_i^*)$ are the mathematical expectation and variance of G_i^* respectively, and W_{ij} is the spatial weight. If $Z(G_i^*)$ is positive, a higher value indicates that the higher value around the i-th raster belongs to the spatial aggregation area, i.e., a hot-spot area. Next, the coordinates of the barycenter of the hot-spot area can be calculated by the following formula:

$$\begin{cases} X_t = \sum_{i=1}^{n} C_{ti}X_{ti} / \sum_{i=1}^{n} C_{ti} \\ Y_t = \sum_{i=1}^{n} C_{ti}Y_{ti} / \sum_{i=1}^{n} C_{ti} \end{cases} \tag{13}$$

where X_t, Y_t are the longitude and latitude of the GBL barycenter in the t-th period respectively, n is the total number of pixels in the GBL hot-spot area in the t-th period, X_{ti}, Y_{ti} are the coordinates of the geometric center of the i-th pixel in the t-th period respectively, and C_{ti} is the GBL probability of the i-th pixel in the t-th period.

3. Results

3.1. Sensitivity and response time of vegetation dynamics to water variability in CA

Vegetation has a hysteresis effect on moisture changes, usually responding to cumulative moisture changes over a period of time rather than instantaneously (Martínez-Vilalta and Lloret, 2016; Vicente-Serrano et al., 2013). The sensitivity and response time of vegetation dynamics to water variability were investigated by separately constructing the correlation between kNDVI and SPEI on different time scales from 1 to 24 months. The authors believe that the greater the correlation, the more sensitive the vegetation is to drought, and the characteristic time scale that achieves maximum kNDVI-SPEI correlation is defined as the vegetation response time to drought.

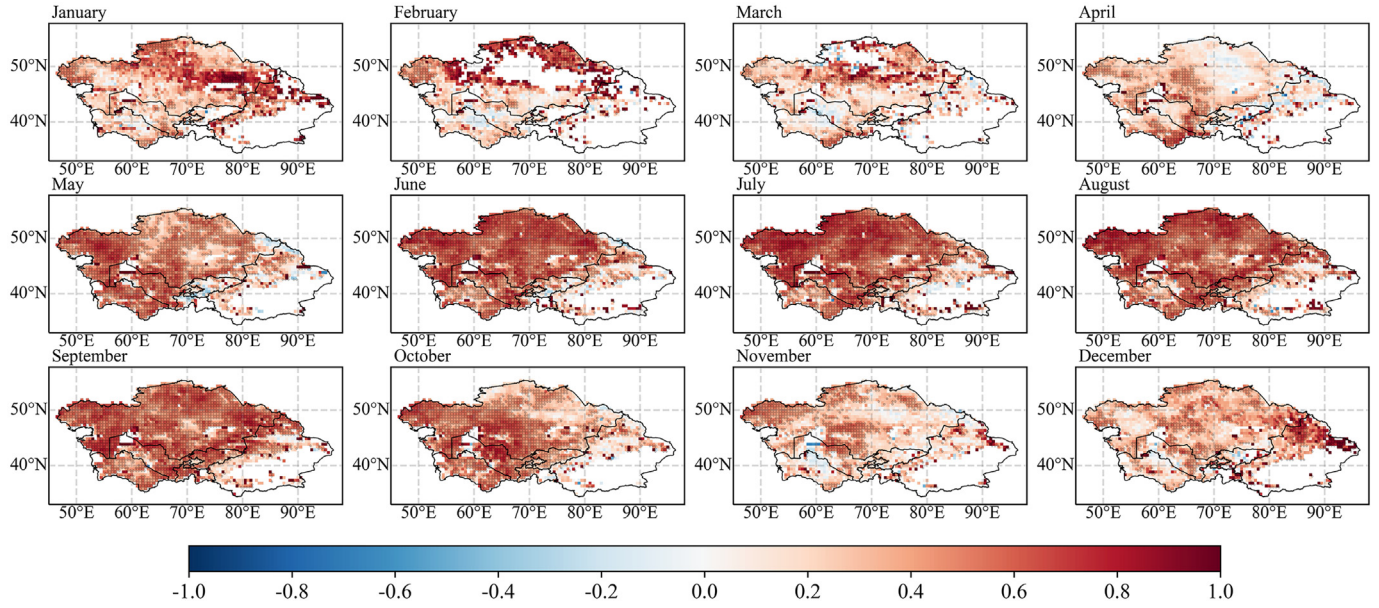

Fig. 3. Spatial distribution of the maximum Pearson correlation coefficients between monthly kNDVI and SPEI at time scales from 1 to 24 months for 1982–2018 for each month. Pixels with significant SPEI-kNDVI correlations (p-value ≤ 0.05) are masked using black dots.

Fig. 3 shows that the CA region as a whole is dominated by a positive correlation between kNDVI and SPEI and that the number of pixels with positive kNDVI-SPEI correlation from January to December was 76.30 % of the total number of pixels. Among them, the largest number of pixels with a positive kNDVI-SPEI relationship occurred in September, accounting for 86.15 % of CA, and the smallest number of positive kNDVI-SPEI pixels occurred in February, accounting for 53.45 % of CA. In terms of time, kNDVI-SPEI correlations were significantly different, with the percentages of pixels with significant positive correlation ($p < 0.05$) all exceeding 50 % of CA and showing an upward trend with a peak in September (69.79 %). In terms of regions with significant correlation, the remaining months accounted for <25 % of the Central Asian region, with an average maximum Pearson correlation coefficient of 0.403, which was down 26.3 % compared to May–October (average maximum Pearson correlation coefficient of 0.509). In addition, a high kNDVI-SPEI correlation also indicated that SPEI could be used as a key indicator of changes in vegetation status, which proved the reliability and rationality of this study. In terms of spatial characteristics, southeastern Xinjiang is composed mainly of bare areas, with sparse vegetation only from May to October and kNDVI-SPEI showing a positive correlation. In particular, the overall kNDVI-SPEI correlation in Xinjiang, involving mainly tree and rangeland distributions, showed a higher positive value than other regions in Xinjiang. However, negative kNDVI-SPEI correlations appeared in March, April, May, and November. Throughout February, March, April, and May, the Central Asian region had a northeast-southwest tilted trend of regional shift in high correlation, and after the beginning of June, most regions showed their peak kNDVI-SPEI correlation during the year. Overall, the kNDVI-SPEI correlations exhibited less spatial heterogeneity and showed higher positive values from May to October, indicating that vegetation dynamics in the Central Asian region are more sensitive to water variability during this period. This correlation analysis shows that monthly-scale temporal variations must be considered when studying the sensitivity of vegetation to moisture changes. Special attention should be paid to the months from May to October, when precipitation shortages and high temperatures can contribute to an increasing shortage of soil moisture, which often triggers a correspondingly dramatic response in vegetation dynamics and leads to GBL.

In addition, different months have different response times of vegetation to water variability. Fig. 4 shows the vegetation response time statistics for each month. It can be seen that the response time follows a decreasing trend from February to May, then stays at a low level from May to October with an average response time of 10 months, and finally starts to rebound in November. From the spatial distribution perspective (Fig. S1), the regions with more abundant vegetation types, found in Xinjiang and at the junction between Kazakhstan and Kyrgyzstan in CA, had a longer response time to water variability from May to October, whereas the northern region, which is dominated by a single vegetation type, showed a short response time. Compared with the vegetation response time in May–August, the vegetation response time in the remaining months was longer (the average response time was 13 months). From the perspective of spatial distribution, the pixels with longer vegetation response time are mainly distributed in the central region. According to the definition in this paper, vegetation response time can reflect the drought resistance of vegetation. Therefore, the longer the vegetation response time, the stronger the drought resistance, and vice versa.

3.2. Various degrees of GBL probability under multiple drought scenarios

To continue the systematic assessment of GBL probability under drought stress and quantify the impact of drought on vegetation health, three drought scenarios were defined in this study: moderate drought, with $-1.5 < SPEI \leq -1$; severe drought, with $-2 < SPI \leq -1.5$; and extreme drought, with $SPEI \leq -2$. To identify drought-vulnerable areas, the probabilities of various degrees of GBL caused by a particular drought must be comprehensively assessed. The degrees of loss were characterized by kNDVI at 0.4, 0.3, 0.2, and 0.1 percentiles in this study. Pixel-by-pixel kNDVI values at the 0.4, 0.3, 0.2, and 0.1 quantiles for Jan to Dec are shown in the Figs. S2 to S13. A low-percentile kNDVI represents a significant reduction in vegetation health and severe damage to terrestrial ecosystems.

The calculated probabilities of different levels of GBL in September under different drought scenarios are shown in Fig. 5, and the results for the remaining months are shown in the Figs. S14 to S24. The Pave value displayed in the upper left corner of each subplot indicates the average GBL probability in the study area. The first column of the subplot of Fig. 5 shows that the mean probabilities of kNDVI below the 0.4 quantile in September were 64.4 %, 71.99 %, and 78.53 % under moderate, severe, and extreme drought conditions respectively. The probability of GBL increased with more severe drought, as was the case when other levels of GBL occurred. In terms of probability differences, the probability of kNDVI decreasing to the 0.4 quantile under the moderate drought scenario

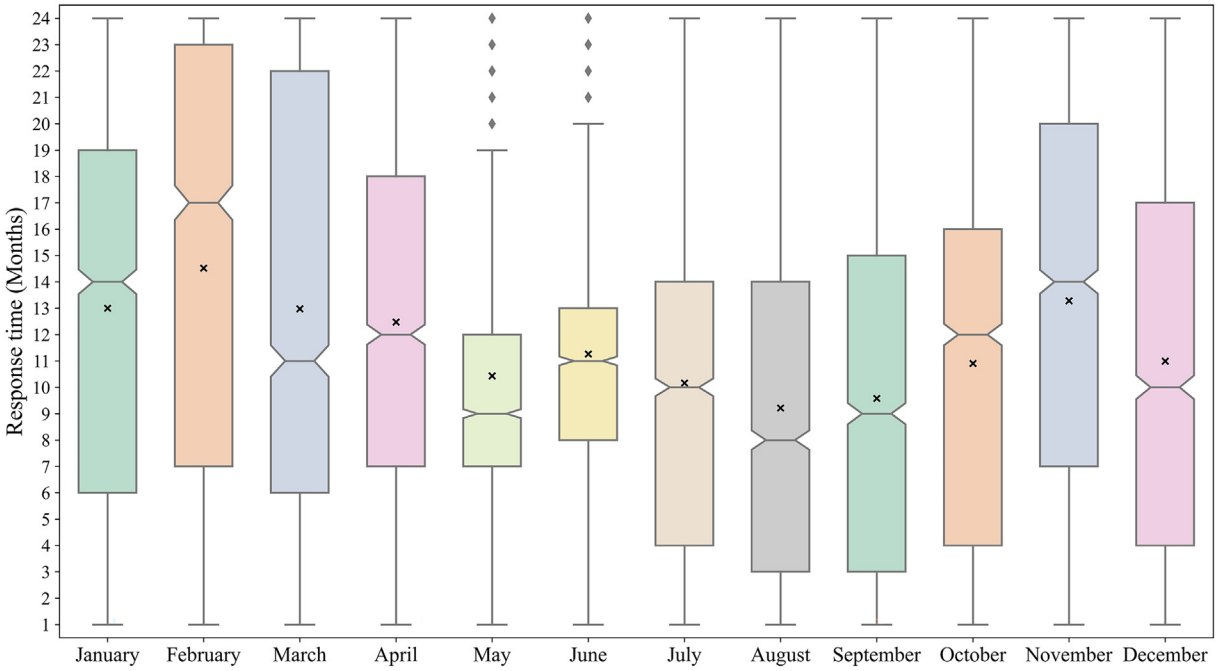

Fig. 4. Box plot showing vegetation response time to water variability in each month. A colored box indicates the interquartile range, with the enclosed horizontal line being the median. Upper and lower whiskers indicate the 90th and 10th percentiles, and mean values are represented by crosses.

(64.4 %) differed from the probability of kNDVI decreasing to the 0.4 quantile under the extreme drought scenario (78.53 %) by 14.13 %. The percentage-point difference in probability increased to 18.09 % under the moderate and extreme drought scenarios and to 21.24 % and 21.09 % when kNDVI was at the 0.3, 0.2, and 0.1 quantiles. Similar variation patterns were observed in other months, as shown in the accompanying figure. The above quantitative probability analysis indicates a positive response of GBL probability to the severity of water scarcity, and that vegetation vulnerability increases with more severe drought in the Central Asian region. As for time scale, under moderate, severe, and extreme drought, the mean probabilities of kNDVI being below the 0.4 quantile were 62.67 %, 70.04 %, and 76.24 % in May–October respectively, and were significantly higher than their values in the remaining months (49.60 %, 50.73 %, and 54.58 % respectively), with the highest probability of kNDVI below the 0.4 quantile occurring in August (65.91 %, 73.89 %, and 80.45 % respectively). The average probability of loss in May–October was also significantly higher than in the remaining months when kNDVI was at the 0.3, 0.2, and 0.1 quantiles, and the GBL probability in August remained the highest, indicating that the CA showed the highest probability of GBL in August and exhibited the strongest vulnerability (Fig. S21).

Analyzing the spatial heterogeneity of GBL probabilities and identifying drought-vulnerable ecosystems can help in accurate drought preparedness and risk management. Fig. 5 clearly shows that the spatial variation of GBL probabilities of the same degree becomes more and more obvious as drought intensifies. As shown in Fig. 5(a), the spatial variability of the probabilities when kNDVI is at different quantiles under the moderate drought

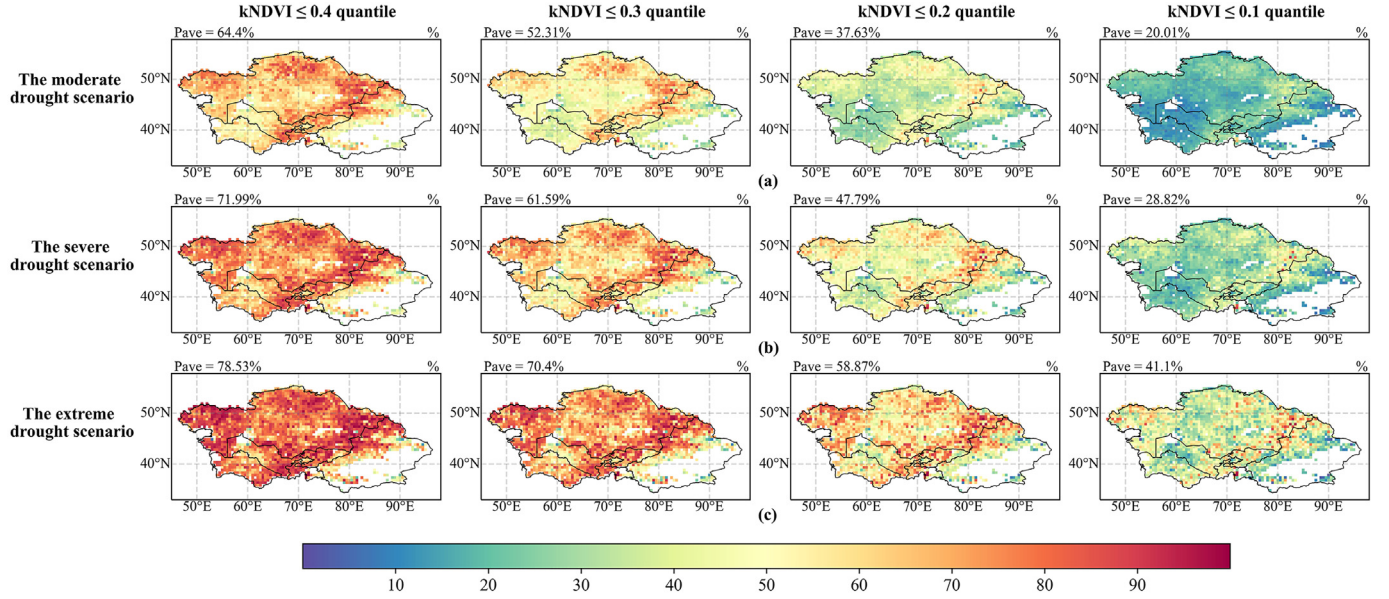

Fig. 5. Conditional probabilities of deteriorating vegetation status (i.e., 40th, 30th, 20th, and 10th percentiles of the kNDVI records) given (a) moderate drought, (b) severe drought, and (c) extreme drought in September.

scenario is not obvious, with similar likelihood of suffering the same degree of vegetation damage. This scenario does not make it easy to identify drought-vulnerable areas. However, spatial variability becomes increasingly evident as drought progresses to severe and extreme levels, especially in the scenario near the lower right corner in Fig. 5. Because a greater probability of GBL was found in August, Fig. S21 was used to identify drought-vulnerable areas. The results showed that drought-vulnerable zones in the study area are mainly distributed over parts of the northern edge of Central Asia, mainly in Kazakhstan and along the northwestern edge of Xinjiang. In general, ecosystems in arid regions have higher vulnerability when subjected to drought stress, and drought-vulnerable areas tend to expand when the amount of water required for vegetation growth increases. It is noteworthy that the drought-vulnerable areas that were screened based on conditional probabilities are in good agreement with those maintaining high kNDVI-SPEI correlation, thus demonstrating the potential of the kNDVI-SPEI correlation coefficient as an effective indicator of vegetation vulnerability assessment. This study provides a theoretical basis for spatial mapping of drought-vulnerable ecosystems in CA, which is important for good and effective drought preparedness and risk management.

3.3. Probabilities of GBL under future trend changes of drought

A link has been constructed between kNDVI and SPEI based on copula theory, and arid and vulnerable areas in CA have been identified based on historical monitoring data. However, under the general trend of global climate change, drought may have devastating effects on regional vegetation, water resources, and the ecological environment. Therefore, in the context of rapid warming, it is particularly important to accurately predict the trend of future drought changes and their impact on vegetation. In this section, based on the climate change scenario data (SSP126, SSP245, SSP585) of the three CMIP6 shared socioeconomic pathways, SPEI values on a 12-month time scale were selected to predict future drought trends in Central Asia and to further identify drought-vulnerable areas under future climate change scenarios.

As shown in Fig. 6(a), the SPEI distribution during 1982–2018 and the SPEI distribution under the SSP245 scenario are more concentrated and single-peaked, whereas the SPEI distributions under the SSP126 and SSP585 scenarios are more dispersed and double-peaked. From the SPEI distribution, compared with the historical scenarios, the SPEI values under the SSP126 and SSP245 scenarios are large, and the SPEI values under the SSP585 scenario are small. Combined with the Fig. 6(b-d) linear variation plot, the SPEI showed a significant decreasing trend under the high-forcing (SSP585) scenario, and the drought intensified with time. The drought intensity increased slightly under the low-forcing (SSP126) and moderate radiative forcing (SSP245) scenarios, and the drought intensification trend was more stable. In addition, it can also be seen from Fig. 6 that the change trend of drought in the two periods before and after 2060 has a certain difference. After 2060, the SPEI values under the three SSP scenarios fluctuated greatly, and the aridification was further aggravated. Therefore, in the subsequent research process, we use 2060 as the cut-off year to divide the future period into two periods for analysis, namely the near future period (NFP, 2019–2060) and the far future period (FFP, 2061–2100).

In addition, based on Sen's slope of drought trends and the Mann-Kendall significance test with a 0.05 significance level, the spatial distribution characteristics of past and future drought change trends in CA were also analyzed (Fig. S25). From these spatial distributions, the percentage of the area with enhanced drought changes in the CA region during 1982–2018 was 78.2 %, and most of Xinjiang and the western part of CA showed a significantly enhanced drought change trend. Under future climate change trends, the spatial distribution patterns of future drought change trends under the three shared socioeconomic pathways were basically consistent, and the spatial distributions of dry and wet change trends were also relatively concentrated and clear. Under the low-forcing scenario, the magnitude of future drought change was smaller and more unstable, with only 44.5 % of the regions showing a significantly enhanced drought change trend. In terms of trend values, the regional values of Sen for SSP126, SSP245, and SSP585 were 6.3×10^{-5}/year, 18.4×10^{-5}/year, and 31.3×10^{-5}/year respectively. The increases were roughly exponential, which further demonstrates that the arid regions of Central Asia will remain at risk of future droughts and that controlling global warming by reducing greenhouse gas emissions is critical. Note that under the three climate change scenarios with different emission intensities, drought changes in most areas of Xinjiang showed a significantly enhanced trend, and most of the intensified drought areas were bare land. This indicates that in the climate change context, the decrease of precipitation and the increase of potential evapotranspiration in global drylands in the future may lead to further intensification of drought conditions and expansion of arid zones in drylands, as well as threatening rangelands and woodlands in the surrounding areas and enhancing ecosystem vulnerability.

To quantify changes in the vulnerability of Central Asian regional ecosystems under future climate change scenarios, the GBL probabilities at the 0.4, 0.3, 0.2, and 0.1 quantiles of kNDVI were calculated for the two future periods under the three future climate change scenarios based on the copula relationship between kNDVI and SPEI established in the previous section. Fig. S28 shows the calculated results for the high-emission scenario

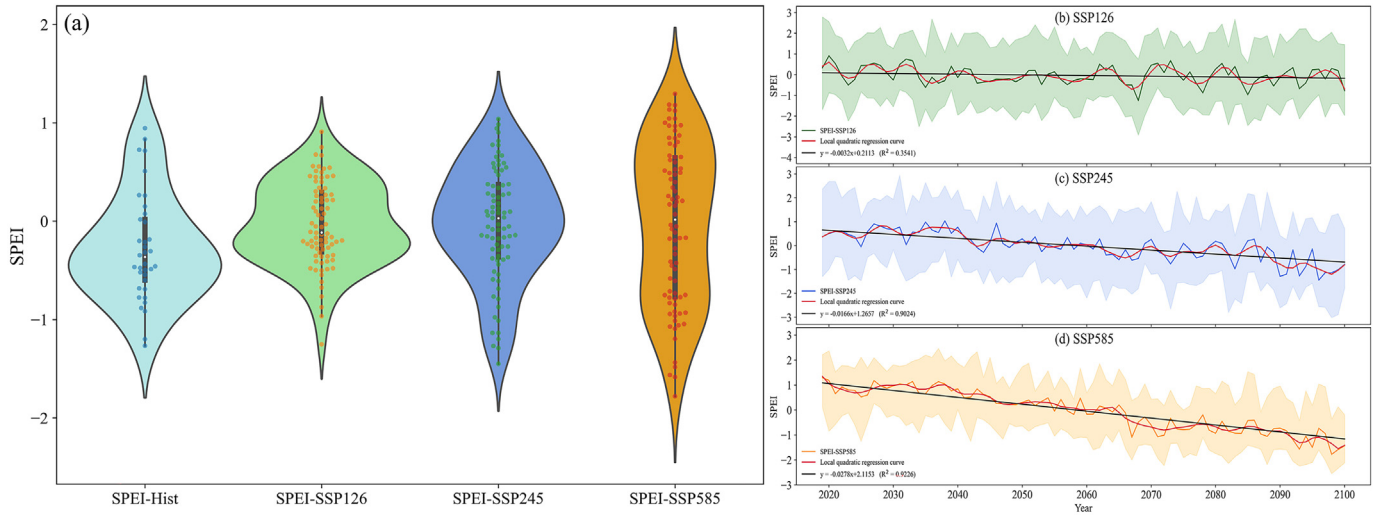

Fig. 6. Drought trends under SSPs. (a) Violin and swarm diagrams showing the distribution of SPEI-12 for a recent historical period (1982–2018) and three future paths (2019–2100) under SSP126, SSP245, and SSP585. (b)-(d) Temporal evolution of SPEI-12 for the three future paths; the colored lines represent the mean SPEI-12 in 2019–2100 under the SSPs; the shadow represents the range of SPEI-12 in each year. The solid black line indicates the linear trend line, and the smoothed line based on local quadratic regression is marked with a dashed crimson line.

(SSP585). In terms of time, for different degrees of GBL, the probability of GBL in the FFP was greater than in the NFP, and the percentage-point differences in probability between the two periods were 18.41 %, 15.13 %, 11.61 %, and 6.74 % respectively. This represents a decrease in probability difference with increasing degree of GBL. For the same future periods, the GBL probability was greatest when kNDVI was at the 0.4 quantile (39.41 % and 57.82 % respectively) and tended to decrease with increasing degree of GBL. The same phenomenon was found under the SSP126 and SSP245 scenarios (as shown in the Figs. S26 to S27), with significant differences in the likelihood of GBL in the FFP versus the NFP. Future vegetation vulnerability was further enhanced under all three SSP scenarios, and the drought-vulnerable area further expanded spatially, yet the spatial distribution of GBL probabilities did not exhibit significant spatial heterogeneity under all three SSP scenarios, either in the far future or in the near future. Therefore, the conditional probabilities when kNDVI was below average under the three SSP scenarios (as shown in Fig. 7) were also calculated. There was no significant difference in the GBL probability between 2019 and 2060 and 2061–2100 under the low-emission scenario (Fig. 7a), and the percentage-point difference in probability between the two periods was 0.38 %. In contrast, the GBL probability in the FFP was significantly larger than in the NFP under the medium- and high-emission scenarios (Fig. 7b-c). Combined with the drought change trends shown in Fig. S25, these results indicate that the GBL probability will further increase as future droughts become more intense. The spatial distribution of GBL probabilities under different scenarios varied significantly, and most regions in Xinjiang and Kazakhstan remained drought-vulnerable areas that will need attention in the future. It is noteworthy that relatively low GBL probabilities were found near the Aral Sea.

4. Discussion

4.1. GBL caused by drought in CA: from a probabilistic perspective

Central Asia, with scarce average multi-year precipitation and high evapotranspiration, is a region with severe water shortages, and the aggravation of drought caused by unreasonable water management systems poses a great threat to the ecological environment (Bai et al., 2019; Wilhite, 2000). Previous studies found that precipitation is the dominant factor controlling vegetation dynamics in CA (Jiang et al., 2017), and therefore this study assessed vegetation vulnerability using the degree of drought as a priori condition. The sensitivity and response time of vegetation to water changes were examined by establishing the relationship between kNDVI and SPEI at different time scales. The results showed that a dependence of vegetation dynamics on fluctuations in water availability was observed in most areas (the percentage of pixels with a positive kNDVI-SPEI relationship was 76.3 %, Fig. 3). Vegetation dynamics in CA are dominated by changes in moisture, mainly due to the water constraint on vegetation phenological and physiological processes such as seed germination, photosynthesis, and carbon and nitrogen use (Rotenberg and Yakir, 2010; Vicente-Serrano et al., 2013). In addition, vegetation growth from May to October was found to be more sensitive to water variability (average correlation coefficient between kNDVI and SPEI was 0.509, Fig. 3). Compared with other months, vegetation was in its fastest growth period and needed a large water supply to maintain it. However, rainfall shortage and concurrent high temperature stress caused severe water shortage in atmospheric evaporation demand, which more strongly inhibited the photosynthesis and respiration rate necessary for leaf growth and maintaining green vegetation (Martínez-Vilalta and Lloret, 2016). At the same time, due to the increasing water demand of plant growth, leaf enlargement, reproduction, and cooling during this period, the sensitivity of vegetation to water shortage increased in a short period of time (Jiao et al., 2021), and therefore a shorter response time was found from May to October (10 months on average, Fig. 4). Notably, in areas with more abundant vegetation types in central CA, the vegetation dynamics were found to respond over a longer time to water changes from May to October. In general, the richer the vegetation types, the stronger will be their resistance to fluctuations in water variability (Martínez-Vilalta and Lloret, 2016; Vicente-Serrano et al., 2013), and long-term water shortages will not have much impact on the local vegetation in a short time. CA is an arid and semi-arid region with perennial drought and low rainfall, where vegetation has been affected by water scarcity for a long time and has evolved physiological mechanisms to cope with

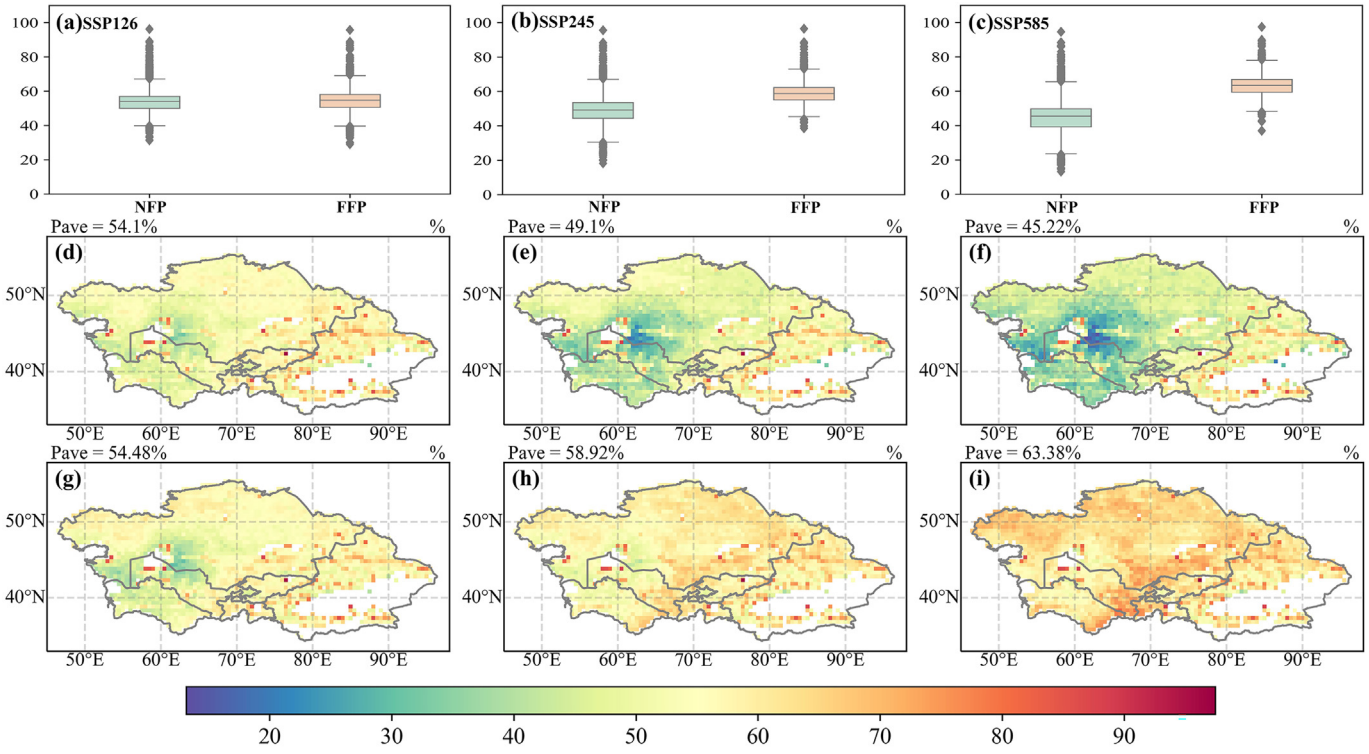

Fig. 7. Conditional probabilities of below-average kNDVI given drought conditions for two future cycles (2019–2060 (d), (e), (f) and 2061–2100 (g), (h), (i)) under the SSP126 (d), (g), SSP245 (e), (h), and SSP585 (f), (i) scenarios.

water scarcity (including more efficient water storage systems and deeper root systems) to adapt to the adverse conditions (Bai et al., 2019; Jiang et al., 2019). These physiological mechanisms help to mitigate the negative effects of short-term water shortages on vegetation dynamics, resulting in a vegetation response over a longer time scale. In summary, when studying the sensitivity of vegetation to water variability, monthly-scale temporal variation must be considered. Relevant agency personnel should pay particular attention to the May–October period, when precipitation shortages and high temperatures can drive soil moisture toward an increasing shortage condition, which often triggers a correspondingly dramatic vegetation response dynamic, leading to GBL (Yang et al., 2019).

Notably, the vegetation response time in this study was derived from a Pearson correlation analysis that comprehensively quantified the association between vegetation dynamics and water deficit or surplus. However, the kNDVI-SPEI correlation results shown in Fig. 3 could not explain whether water deficit or water surplus caused the vegetation dynamic changes. At the current stage, there is still a lack of quantitative understanding of whether water deficit or water surplus plays a more critical role in weakening vegetation health in CA (Fang et al., 2019b; Mankin et al., 2019).

This study used a binary probabilistic framework based on copula theory to address this issue by comparing the probability of GBL (measured by kNDVI being below the monthly average) under drought and wet conditions to improve the importance of our study of vegetation vulnerability under drought stress. The monthly conditional probabilities that kNDVI was lower than average under dry conditions (SPEI ≤ -0.05) and under wet conditions (SPEI ≥ 0.5) were calculated, and as well as the difference between them ($P(kNDVI<kNDVIave \mid SPEI) \leq -0.05) - P(kNDVI < kNDVIave \mid SPEI \geq -0.05)$). The results are shown in Fig. 8, where positive values indicate that GBL is mainly caused by water deficit, that is, vegetation is more vulnerable when water is scarce, and vice versa. In terms of averages, 94.4 % of the regions had a positive percentage-point probability difference of 44.6 % on average from May to October, and 74.2 % of the regions had a positive percentage-point probability difference of 15.3 % in the remaining months. This indicates that the positive probability difference is dominant in the CA region, that vegetation is more vulnerable under dry conditions than under wet conditions, and that water deficit rather than excess water plays a more important role in inhibiting vegetation dynamics. However, it should also be noted that from January to April and in November and December, GBL in northern CA may be attributed to a water surplus. This occurs when vegetation health is low, water demand is low, and either solid or liquid precipitation causes a decrease in soil temperature, which inhibits the recovery of sparse vegetation (Su et al., 2011). The same phenomenon was found in the Altay region of Xinjiang and in the Tarim River Basin during May–October. Studies have shown that precipitation is the leading factor affecting vegetation growth in the Altay mountainous area (Jiang et al., 2017). Although the average annual precipitation in Altay has been increasing in recent years, the temporal distribution of rainfall has changed from a uniform distribution to concentrated events, and the frequent occurrences of extreme rainfall events are likely to flood plants (Martínez-Vilalta and Lloret, 2016). Excessive soil moisture during flooding can lead to anaerobic respiration of plant roots, which affects plant nutrient and water uptake efficiency, causing stunted growth and even death (Martínez-Vilalta and Lloret, 2016). This is also the main cause of GBL due to water surplus in the Tarim River Basin. To repair and rebuild the ecological environment of the Tarim River downstream, the Tarim River Basin Comprehensive Management Project was started in 2000, with ecological water transfer to the lower reaches by ecological sluice control and near-natural overflow (Ling et al., 2019). By the end of December 2020, twenty-one ecological water transfers had been made to the Tarim River downstream, mostly from April to November each year, with a total of 84.45 × 10^8 m^3 of water transferred (Huang and Pang, 2010). However, the variation of water delivery from year to year has been large, with the maximum delivery being 12.15 × 10^8 m^3 in 2017, and a large amount of water is delivered to the vegetation through diffuse overflow, leading to flooding (Ling et al., 2019). These findings indicate that both water surplus and water deficit lead to increased vegetation vulnerability, and that therefore, in water-scarce arid zones, an integrated consideration of efficient water utilization plays an important role in maintaining the functional stability of ecosystems.

4.2. Migration trajectory of GBL barycenter and coping strategies in CA

In the context of global warming, the severity and impact of future droughts will tend to increase (Gampe et al., 2021; Trenberth et al., 2014) in the context of global warming. Frequent droughts will cause more negative impacts on ecosystems, and quantitative understanding of vegetation vulnerability under drought stress and mapping the spatial distribution of drought-vulnerable areas are essential for drought preparedness and mitigation (Jiao et al., 2021). Based on historical observations and BCC-CSM2-MR climate model data, using a binary-probability framework based on copula theory, this study has quantified the GBL

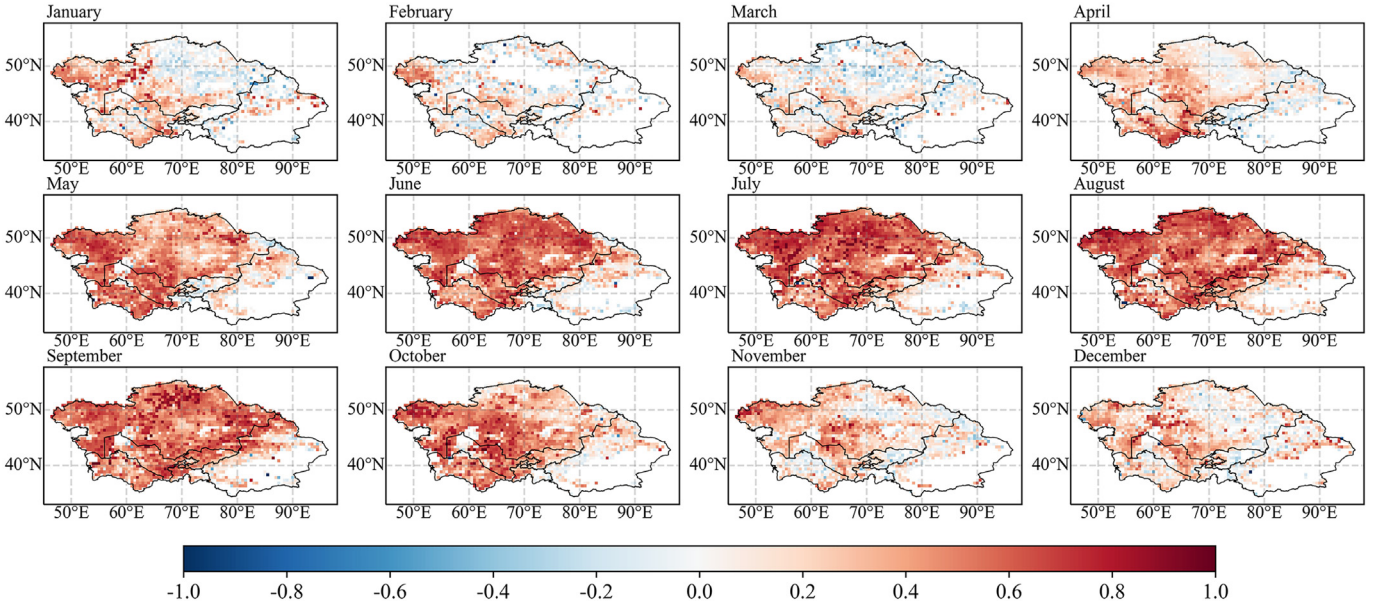

Fig. 8. Difference in probabilities of below-average GBL under dry and wet conditions for each month.

probabilities for both historical and future periods. For the historical period, the conditional probabilities when four levels of GBL occurred in different months under three drought scenarios were calculated. As shown in Fig. 5, the average percentage GBL under extreme drought scenarios was as high as 44.66 % when severe ecosystem damage occurred. The probability of GBL in CA under different drought-GBL combinations reaches its peak in August; the drought-vulnerable areas are mainly located in parts of the northern edge of CA, including Kazakhstan and the northwestern edge of Xinjiang, China. The future period was divided into a near-future period (NFP, 2019–2060) and a far-future period (FFP, 2061–2100) based on the difference in future drought change trends. In the context of the SSP126, SSP245, and SSP585 scenarios, the maximum percentage-point differences in the probability of GBL between the NFP and the FFP when kNDVI was below average were 0.38 %, 9.82 %, and 18.16 % respectively, which indicates that vegetation vulnerability will further increase in the future. From the spatial distributions, most regions in Xinjiang and some regions in Kazakhstan are still drought-vulnerable areas that need attention in the future. The results show that the possibility of GBL responds positively to the severity of water scarcity. In addition to the impact of water resources, this study also explores the impact of local soil water storage and temperature on vegetation growth. The soil water storage data is derived from the GLDAS_NOAH 2.0 dataset (Zhang et al., 2021), the temperature data comes from the CRU_TS 4.06 dataset (Harris et al., 2020). From Fig. S29, it can be seen that 84.66 % of the regional soil water storage in CA shows an upward trend, of which 68.23 % show a significant upward trend, mostly concentrated in the northwest of CA. The soil water storage in some areas at the junction of Kazakhstan and Xinjiang, China showed a slight downward trend. On the whole, the soil water storage in CA also showed an upward trend from 1982 to 2018 (Fig. S31). The soil water storage directly affects the growth and development of vegetation, so the increase of soil water storage has a promoting effect on the growth of vegetation (Querejeta, 2017). Fig. S30 shows that the temperature of 98.33 % of the CA region shows a significant upward trend, and the temperature increase in the western CA and Xinjiang region of China is larger. Fig. S32 shows that vegetation has an obvious feedback effect on the change of temperature. Higher or lower temperature will inhibit the growth of vegetation, and kNDVI increases with the increase of temperature within a certain temperature range (He et al., 2022; Kang et al., 2021). In addition, it can be seen that the increase in temperature is one of the direct causes of drought, and Fig. S25(a) also shows that the trend of drought strengthening in western CA and Xinjiang, China is more obvious than other regions. The above analysis deepens the response mechanism of vegetation to drought understanding. With more intense drought, the probability of GBL is also increasing, and the drought-vulnerable area will further expand. The main effect of drought on vegetation growth is water stress, and when the duration and intensity of drought reach a certain level, it can cause serious damage to the growth and physiological functions of vegetation and even lead to the death of a large number of individual plants (Jiao et al., 2021; Li et al., 2019).

Based on three typical CMIP6 SSPs, this study used SPEI to predict future drought conditions in CA. The results show that with increasing SSPs and warming, the magnitude and intensity of droughts increase significantly, with 44.5 %, 95.7 %, and 100 % of the regional drought changes showing a significantly enhanced trend under the SSP126, SSP245, and SSP585 scenarios respectively (Fig. S25). CA still faces a more severe drought threat in the future. However, a smaller probability of GBL was found in the Aral Sea region (Fig. 7). The Aral Sea basin is located in the arid zone of the Asian continent, where population growth and irrational use of soil and water resources have led to serious problems of land desertification, soil erosion, and environmental pollution (Jiang et al., 2020b; Wu et al., 2020). The Aral Sea crisis has been called 'the greatest environmental disaster of the 20th Century'. Since the 1990s, the establishment of the International Aral Sea Rescue Organization has made great contributions to solving the problems of land loss and inefficient water resources utilization in the Aral Sea Basin, and has achieved certain results (Wu et al., 2020). In addition, the Chinese government proposed in 2016 to integrate the construction of the "Silk Road Economic Belt" with the ecological protection of Central Asia and came up with its own plan to solve the Aral Sea crisis. The findings of this study based on the future SSP climate change scenarios in the Aral Sea region give us reason to believe that in the future, the Aral Sea crisis will be significantly mitigated under the intervention of human policy. From the above research results, it can be concluded that to cope with the challenges brought by climate change in the future, it is urgent to build a community with a shared future for mankind and to carry out international cooperation in disaster management from the perspective of the sustainable development of global human society.

The barycenter migration model is an effective method to respond to the evolution of objects in space and is widely used in many studies of spatial processes and patterns (Jiang et al., 2020a). This study used a barycenter migration model to map the shift paths of the center of gravity of GBL in the historical and future periods under three climate change scenarios, which helps to further quantify the spatial distribution characteristics of drought-vulnerable areas. This information is of great significance for governments and relevant staff at all levels to grasp drought information in a timely manner, formulate measures for drought prevention and mitigation, and realize the transformation from emergency management to risk management of drought disasters (Hu et al., 2019; Jiang et al., 2020a). The spatial pattern of barycenter shift (Fig. 9) shows that the GBL barycenter shifts significantly over the three periods, mainly in Kazakhstan and Xinjiang. Under the three SSP scenarios, the shifting trends of GBL barycenter from historical period to NFP and from NFP to FFP were basically the same. From the perspective of the migration trajectory of the barycenter, in all three scenarios, it moves from the central part of Kazakhstan to the southeast, and then moves to the northwest. From the historical period to the NFP, the barycenter shows a northwest-southeast trajectory, but from the NFP to the FFP, it shows a southeast-northwest trajectory. The barycenter migration distance is the longest in the high-emission scenario. It is worth noting that the GBL barycenter in the NFP under the low-emission and high-emission scenarios is in Xinjiang, and in the three scenarios, the GBL barycenter from the historical period to the NFP stage develops toward Xinjiang. However, in the FFP, the barycenter moves in the opposite direction. The SSP future climate change scenarios used in this study are based on descriptions that can characterize future socio-economic development trends, incorporate factors such as population, economic growth, education, urbanization, and technological development rates, and consider the climate policies that countries have already adopted (Riahi et al., 2017; Wigley and Raper, 1992). As a country with a large economy and population, China has been working hard to deal with global climate change, energy conservation and emission reduction (Niu et al., 2011). As early as 2006, China put forward the strategic goal of energy conservation and emission reduction, and then at the 75th United Nations General Assembly China proposed Aim for carbon neutrality by 2060 (Ma et al., 2020; Zhao et al., 2022). This paper divides 2060 into time nodes in the near-future and far-future periods according to the difference in future drought trends. The results show that in the FFP, the GBL barycenter in CA tends to shift from Xinjiang, China to the northwest, which indicates that the GBL barycenter in CA has shifted due to some reasons in the far future. However, we should also realize that in the near future, the GBL barycenter in CA is located in Xinjiang, China, and relevant staff still need to focus on the Xinjiang region and take precautionary measures to deal with future droughts.

5. Conclusion

To test the scientific hypothesis that aggressive climate change coping strategies can shift the migration trajectory of the GBL barycenter due to drought, a binary probabilistic framework was constructed based on copula theory. Calculations showed that 62.6 % of the regional maximum kNDVI-SPEI correlations in CA reached a significant level ($p < 0.05$) in May–October on average, indicating a high sensitivity of vegetation to drought. Using this framework, the study found that an average of 94.4 % of regional GBL in May–October was caused by water deficit. From the perspective of

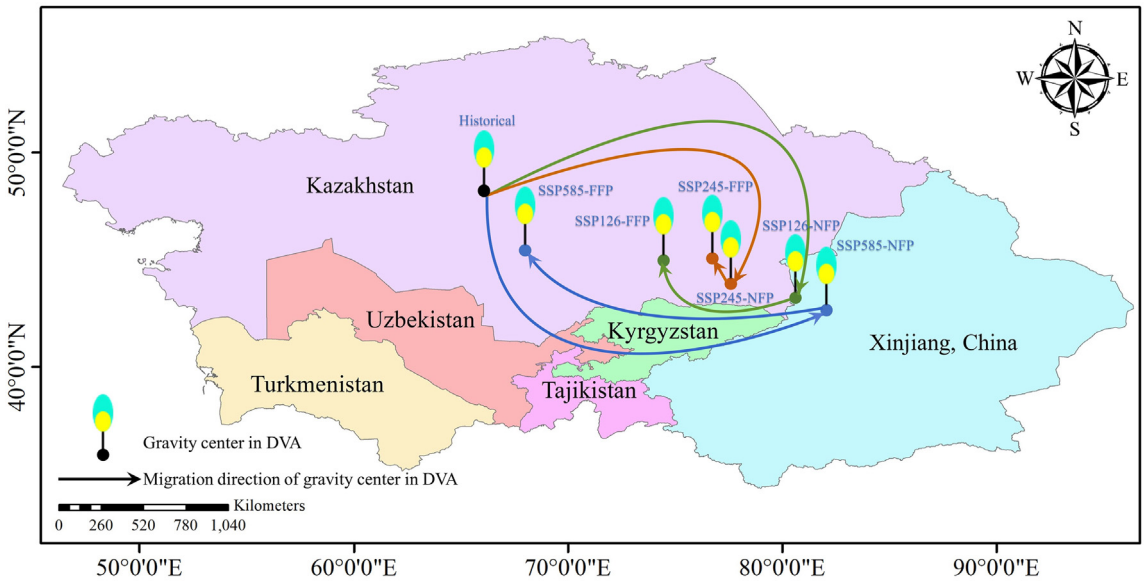

Fig. 9. Migration trajectory of GBL barycenter in CA. 'Historical' refers to the GBL barycenter in historical periods, 'SSP126-NFP' refers to the GBL barycenter in the NFP under the SSP126 scenario; 'SSP126-FFP' refers to the GBL barycenter in the FFP under the SSP126 scenario; 'SSP245-NFP' refers to the GBL barycenter in the NFP under the SSP245 scenario; 'SSP245-FFP' refers to the GBL barycenter in the FFP under the SSP245 scenario; 'SSP585-NFP' refers to the GBL barycenter in the NFP under the SSP585 scenario; 'SSP585-FFP' refers to the GBL barycenter in the FFP under the SSP585 scenario.

probability, the GBL probability when kNDVI was at 0.4, 0.3, 0.2, and 0.1 quantiles peaked in August (80.45 %, 73.03 %, 62.15 %, and 44.66 % in extreme drought scenarios), with the most severe vegetation vulnerability during this period. Studies show that with more intense drought, the spatial differences in the probability of GBL to the same degree in different months became more and more obvious, and therefore the factors of the variation of GBL probability at monthly scale should be considered when conducting vegetation vulnerability assessment in the future. Thereafter, based on projected future drought trends, the regional values of Sen for the SSP126, SSP245, and SSP585 scenarios were 6.3×10^{-5}/year, 18.4×10^{-5}/year, and 31.3×10^{-5}/year respectively. The percentages of pixels with a significantly increasing drought trend were 44.5 %, 95.6 %, and 100 % respectively. The percentage-point differences in the probability of drought with a significantly enhanced trend in the NFP and the FFP when kNDVI was below average were 0.38 %, 9.82 %, and 18.16 % respectively, indicating that more intense drought under strong emissions stress will increase the probability of GBL. Therefore, measures such as active energy conservation and emissions reduction should be taken to mitigate drought in the future. This effect was also reflected in the trajectory of the GBL barycenter shift. For example, in the high-emission scenario, the GBL barycenter in the NFP was in Xinjiang. However, due to the Chinese government's active measures to respond to global climate change (such as proposing "carbon neutrality" in 2060), the barycenter shifted away from Xinjiang in the FFP. These results not only deepen our knowledge about the feedback mechanism of terrestrial vegetation to drought hazards, but also provide a new idea for the study of GBL laws under global climate change, and can also reference the policies such as energy conservation and emissions reduction issued by the Chinese government to cope with future ecological crises caused by water shortage in arid areas.

CRediT authorship contribution statement

Feifei Han took the lead in writing the manuscript and conducted the data analysis. Feifei Han, Hongbo Ling and Mingjiang Deng conceived of the presented idea and organized the outline. Feifei Han, Junjie Yan and Wenqi Wang contributed to the presentation of the results. Feifei Han, Hongbo Ling, Xiaoya Deng and Yanming Gong contributed to the writing of the article and reviewed the results.

Data availability

Data will be made available on request.

Declaration of competing interest

The authors declare that they have no conflict of interest.

Acknowledgments

This research was funded by the National Natural Science Foundation of China (52179028), the West Light Foundation of Chinese Academy of Sciences (2019-XBQNXZ-A-001), and the Xinjiang Water Conservancy Science and Technology Special Fund Project (XSKJ-2022-10).

Appendix A. Supplementary data

Supplementary data to this article can be found online at https://doi.org/10.1016/j.scitotenv.2022.157656.

References

Abdelmalek, M.B., Nouiri, I., 2020. Study of trends and mapping of drought events in Tunisia and their impacts on agricultural production. Sci. Total Environ. 734, 139311.
Ahmad, T., 2017. Non-technical loss analysis and prevention using smart meters. Renew. Sust. Energ. Rev. 72, 573–589.
Bachmair, S., Svensson, C., Hannaford, J., Barker, L., Stahl, K., 2016. A quantitative analysis to objectively appraise drought indicators and model drought impacts. Hydrol. Earth Syst. Sci. 20, 2589–2609.
Bai, J., Shi, H., Yu, Q., Xie, Z., Li, L., Luo, G., et al., 2019. Satellite-observed vegetation stability in response to changes in climate and total water storage in Central Asia. Sci. Total Environ. 659, 862–871.
Beguería, S., Vicente-Serrano, S.M., Reig, F., Latorre, B., 2014. Standardized precipitation evapotranspiration index (SPEI) revisited: parameter fitting, evapotranspiration models, tools, datasets and drought monitoring. Int. J. Climatol. 34, 3001–3023.
Borgomeo, E., Farmer, C.L., Hall, J.W., 2015. Numerical rivers: a synthetic streamflow generator for water resources vulnerability assessments. Water Resour. Res. 51, 5382–5405.
Borrelli, P., Robinson, D.A., Panagos, P., Lugato, E., Yang, J.E., Alewell, C., et al., 2020. Land use and climate change impacts on global soil erosion by water (2015–2070). Proc. Natl. Acad. Sci. 117, 21994–22001.
Bryan, B.A., Gao, L., Ye, Y., Sun, X., Connor, J.D., Crossman, N.D., et al., 2018. China's response to a national land-system sustainability emergency. Nature 559, 193–204.

Camps-Valls, G., Campos-Taberner, M., Moreno-Martínez, Á., Walther, S., Duveiller, G., Cescatti, A., 2021. A unified vegetation index for quantifying the terrestrial biosphere. Sci. Adv. 7, eabc7447.
Chen, T., Bao, A., Jiapaer, G., Guo, H., Zheng, G., Jiang, L., et al., 2019. Disentangling the relative impacts of climate change and human activities on arid and semiarid grasslands in Central Asia during 1982–2015. Sci. Total Environ. 653, 1311–1325.
Chen, T., Tang, G., Yuan, Y., Guo, H., Xu, Z., Jiang, G., et al., 2020. Unraveling the relative impacts of climate change and human activities on grassland productivity in Central Asia over last three decades. Sci. Total Environ. 743, 140649.
Christian, J.I., Basara, J.B., Hunt, E.D., Otkin, J.A., Furtado, J.C., Mishra, V., et al., 2021. Global distribution, trends, and drivers of flash drought occurrence. Nat. Commun. 12, 1–11.
Dai, A., 2013. Increasing drought under global warming in observations and models. Nat. Clim. Chang. 3, 52–58.
Dalal, A., Bourstein, R., Haish, N., Shenhar, I., Wallach, R., Moshelion, M., 2019. Dynamic physiological phenotyping of drought-stressed pepper plants treated with "productivity-enhancing" and "survivability-enhancing" biostimulants. Front. Plant Sci. 10, 905.
Ding, Y., Xu, J., Wang, X., Peng, X., Cai, H., 2020. Spatial and temporal effects of drought on chinese vegetation under different coverage levels. Sci. Total Environ. 716, 137166.
Drew, M., 1979. Plant responses to anaerobic conditions in soil and solution culture. Commentaries in Plant Science. 2, pp. 209–223.
Fang, Y., Xiong, L., 2015. General mechanisms of drought response and their application in drought resistance improvement in plants. Cell. Mol. Life Sci. 72, 673–689.
Fang, W., Huang, S., Huang, Q., Huang, G., Wang, H., Leng, G., et al., 2019a. Probabilistic assessment of remote sensing-based terrestrial vegetation vulnerability to drought stress of the loess plateau in China. Remote Sens. Environ. 232, 111290.
Fang, W., Huang, S., Huang, Q., Huang, G., Wang, H., Leng, G., et al., 2019b. Bivariate probabilistic quantification of drought impacts on terrestrial vegetation dynamics in mainland China. J. Hydrol. 577, 123980.
Fensholt, R., Proud, S.R., 2012. Evaluation of earth observation based global long term vegetation trends—Comparing GIMMS and MODIS global NDVI time series. Remote Sens. Environ. 119, 131–147.
Fitzsimmons, K.E., Nowatzki, M., Dave, A.K., Harder, H., 2020. Intersections between wind regimes, topography and sediment supply: perspectives from aeolian landforms in Central Asia. Palaeogeogr. Palaeoclimatol. Palaeoecol. 540, 109531.
Gampe, D., Zscheischler, J., Reichstein, M., O'Sullivan, M., Smith, W.K., Sitch, S., et al., 2021. Increasing impact of warm droughts on northern ecosystem productivity over recent decades. Nat. Clim. Chang. 11, 772–779.
Genest, C., Rémillard, B., Beaudoin, D., 2009. Goodness-of-fit tests for copulas: a review and a power study. Insurance Math. Econom. 44, 199–213.
Gocic, M., Trajkovic, S., 2013. Analysis of changes in meteorological variables using mann-kendall and Sen's slope estimator statistical tests in Serbia. Glob. Planet. Chang. 100, 172–182.
Guan, X., Yang, L., Zhang, Y., Li, J., 2019. Spatial distribution, temporal variation, and transport characteristics of atmospheric water vapor over Central Asia and the arid region of China. Glob. Planet. Chang. 172, 159–178.
Harris, I., Osborn, T.J., Jones, P., Lister, D., 2020. Version 4 of the CRU TS monthly high-resolution gridded multivariate climate dataset. Sci. Data 7, 1–18.
He, K., Zhao, W., Brocca, L., Quintana-Seguí, P.S.M.P.D., 2022. A soil moisture-based precipitation downscaling method for high-resolution daily satellite precipitation estimation. Hydrol. Earth Syst. Sci. Discuss. 1–29.
Hofmann, T., Schölkopf, B., Smola, A.J., 2008. Kernel methods in machine learning. Ann. Stat. 36, 1171–1220.
Hu, T., Wu, J., Li, W., 2019. Assessing relationships of ecosystem services on multi-scale: a case study of soil erosion control and water yield in the Pearl River Delta. Ecol. Indic. 99, 193–202.
Huang, T., Pang, Z., 2010. Changes in groundwater induced by water diversion in the lower Tarim River, Xinjiang Uygur, NW China: evidence from environmental isotopes and water chemistry. J. Hydrol. 387, 188–201.
Huang, W., Duan, W., Chen, Y., 2021. Rapidly declining surface and terrestrial water resources in Central Asia driven by socio-economic and climatic changes. Sci. Total Environ. 784, 147193.
Ji, L., Peters, A.J., 2003. Assessing vegetation response to drought in the northern Great Plains using vegetation and drought indices. Remote Sens. Environ. 87, 85–98.
Jiang, L., Bao, A., Guo, H., Ndayisaba, F., 2017. Vegetation dynamics and responses to climate change and human activities in Central Asia. Sci. Total Environ. 599, 967–980.
Jiang, L., Jiapaer, G., Bao, A., Kurban, A., Guo, H., Zheng, G., et al., 2019. Monitoring the long-term desertification process and assessing the relative roles of its drivers in Central Asia. Ecol. Indic. 104, 195–208.
Jiang, F., Zhang, J., Gao, H., Cai, Z., Zhou, X., Li, S., et al., 2020a. Musk deer (Moschus spp.) face redistribution to higher elevations and latitudes under climate change in China. Sci. Total Environ. 704, 135335.
Jiang, L., Bao, A., Yuan, Y., Zheng, G., Guo, H., Yu, T., et al., 2020b. The effects of water stress on croplands in the Aral Sea basin. J. Clean. Prod. 254, 120114.
Jiao, W., Wang, L., Smith, W.K., Chang, Q., Wang, H., D'Odorico, P., 2021. Observed increasing water constraint on vegetation growth over the last three decades. Nat. Commun. 12, 1–9.
Kamp, J., Koshkin, M.A., Bragina, T.M., Katzner, T.E., Milner-Gulland, E.J., Schreiber, D., et al., 2016. Persistent and novel threats to the biodiversity of Kazakhstan's steppes and semi-deserts. Biodivers. Conserv. 25, 2521–2541.
Kang, Y., Guo, E., Wang, Y., Bao, Y., Bao, Y., Mandula, N., 2021. Monitoring vegetation change and its potential drivers in Inner Mongolia from 2000 to 2019. Remote Sens. 13, 3357.
Li, D.X., 2000. On default correlation: a copula function approach. J. Fixed Income 9, 43–54.
Li, X., Li, Y., Chen, A., Gao, M., Slette, I.J., Piao, S., 2019. The impact of the 2009/2010 drought on vegetation growth and terrestrial carbon balance in Southwest China. Agric. For. Meteorol. 269, 239–248.
Li, S., Xiao, W., Zhao, Y., Lv, X., 2020. Incorporating ecological risk index in the multi-process MCRE model to optimize the ecological security pattern in a semi-arid area with intensive coal mining: a case study in northern China. J. Clean. Prod. 247, 119143.
Li, H., Li, Z., Chen, Y., Xiang, Y., Liu, Y., Kayumba, P.M., et al., 2021. Drylands face potential threat of robust drought in the CMIP6 SSPs scenarios. Environ. Res. Lett. 16, 114004.
Ling, H., Guo, B., Zhang, G., Xu, H., Deng, X., 2019. Evaluation of the ecological protective effect of the "large basin" comprehensive management system in the Tarim River basin, China. Sci. Total Environ. 650, 1696–1706.
Lu, Y., Wu, T., Li, Y., Yang, B., 2021. Mitigation of the double ITCZ syndrome in BCC-CSM2-MR through improving parameterizations of boundary-layer turbulence and shallow convection. Geosci. Model Dev. 14, 5183–5204.
Ma, Z., Peng, C., Zhu, Q., Chen, H., Yu, G., Li, W., et al., 2012. Regional drought-induced reduction in the biomass carbon sink of Canada's boreal forests. Proc. Natl. Acad. Sci. 109, 2423–2427.
Ma, M., Ma, X., Cai, W., Cai, W., 2020. Low carbon roadmap of residential building sector in China: historical mitigation and prospective peak. Appl. Energy 273, 115247.
Mankin, J.S., Seager, R., Smerdon, J.E., Cook, B.I., Williams, A.P., 2019. Mid-latitude freshwater availability reduced by projected vegetation responses to climate change. Nat. Geosci. 12, 983–988.
Martínez-Vilalta, J., Lloret, F., 2016. Drought-induced vegetation shifts in terrestrial ecosystems: the key role of regeneration dynamics. Glob. Planet. Chang. 144, 94–108.
Meinshausen, M., Lewis, J., McGlade, C., Gütschow, J., Nicholls, Z., Burdon, R., et al., 2022. Realization of Paris agreement pledges may limit warming just below 2° C. Nature 604, 304–309.
Newbold, T., Hudson, L.N., Hill, S.L., Contu, S., Lysenko, I., Senior, R.A., et al., 2015. Global effects of land use on local terrestrial biodiversity. Nature 520, 45–50.
Niinemets, Ü., Valladares, F., 2006. Tolerance to shade, drought, and waterlogging of temperate northern hemisphere trees and shrubs. Ecol. Monogr. 76, 521–547.
Niu, S., Ding, Y., Niu, Y., Li, Y., Luo, G., 2011. Economic growth, energy conservation and emissions reduction: a comparative analysis based on panel data for 8 asian-Pacific countries. Energy Policy 39, 2121–2131.
Nunez, S., Alkemade, R., Kok, K., Leemans, R., 2020. Potential biodiversity change in central asian grasslands: scenarios for the impact of climate and land-use change. Reg. Environ. Chang. 20, 1–13.
O'Neill, B.C., Tebaldi, C., Van Vuuren, D.P., Eyring, V., Friedlingstein, P., Hurtt, G., et al., 2016. The scenario model intercomparison project (ScenarioMIP) for CMIP6. Geosci. Model Dev. 9, 3461–3482.
Ou, Y., Iyer, G., Clarke, L., Edmonds, J., Fawcett, A.A., Hultman, N., et al., 2021a. Can updated climate pledges limit warming well below 2° C? Science 374, 693–695.
Ou, Y., Roney, C., Alsalam, J., Calvin, K., Creason, J., Edmonds, J., et al., 2021b. Deep mitigation of CO2 and non-CO2 greenhouse gases toward 1.5° C and 2° C futures. Nat. Commun. 12, 1–9.
Pedro-Monzonís, M., Solera, A., Ferrer, J., Estrela, T., Paredes-Arquiola, J., 2015. A review of water scarcity and drought indexes in water resources planning and management. J. Hydrol. 527, 482–493.
Peng, B., Guan, K., Zhou, W., Jiang, C., Frankenberg, C., Sun, Y., et al., 2020. Assessing the benefit of satellite-based solar-induced chlorophyll fluorescence in crop yield prediction. Int. J. Appl. Earth Obs. Geoinf. 90, 102126.
Pinzon, J.E., Tucker, C.J., 2014. A non-stationary 1981–2012 AVHRR NDVI3g time series. Remote Sens. 6, 6929–6960.
Querejeta, J., 2017. Soil water retention and availability as influenced by mycorrhizal symbiosis: consequences for individual plants, communities, and ecosystems. Mycorrhizal Mediation of Soil. Elsevier, pp. 299–317.
Reddy, C.S., Manaswini, G., Satish, K., Singh, S., Jha, C., Dadhwal, V., 2016. Conservation priorities of forest ecosystems: evaluation of deforestation and degradation hotspots using geospatial techniques. Ecol. Eng. 91, 333–342.
Riahi, K., Van Vuuren, D.P., Kriegler, E., Edmonds, J., O'neill, B.C., Fujimori, S., 2017. The shared socioeconomic pathways and their energy, land use, and greenhouse gas emissions implications: an overview. Glob. Environ. Chang. 42, 153–168.
Rotenberg, E., Yakir, D., 2010. Contribution of semi-arid forests to the climate system. Science 327, 451–454.
Salvadori, G., De Michele, C., 2004. Frequency analysis via copulas: theoretical aspects and applications to hydrological events. Water Resour. Res. 40.
Sheffield, J., Wood, E.F., Roderick, M.L., 2012. Little change in global drought over the past 60 years. Nature 491, 435–438.
Sherwood, S., Fu, Q., 2014. A drier future? Science 343, 737–739.
Stagge, J.H., Tallaksen, L.M., Gudmundsson, L., Van Loon, A.F., Stahl, K., 2015. Candidate distributions for climatological drought indices (SPI and SPEI). Int. J. Climatol. 35, 4027–4040.
Su, Z., Wen, J., Dente, L., Van Der Velde, R., Wang, L., Ma, Y., et al., 2011. The tibetan plateau observatory of plateau scale soil moisture and soil temperature (Tibet-Obs) for quantifying uncertainties in coarse resolution satellite and model products. Hydrol. Earth Syst. Sci. 15, 2303–2316.
Sun, G., Wang, C., Chang, L., Wu, Y., Li, L., Jin, Z., 2018. Effects of feedback regulation on vegetation patterns in semi-arid environments. Appl. Math. Model. 61, 200–215.
Tian, L., Yuan, S., Quiring, S.M., 2018. Evaluation of six indices for monitoring agricultural drought in the south-Central United States. Agric. For. Meteorol. 249, 107–119.
Trenberth, K.E., Dai, A., Van Der Schrier, G., Jones, P.D., Barichivich, J., Briffa, K.R., et al., 2014. Global warming and changes in drought. Nat. Clim. Chang. 4, 17–22.
Tucker, C.J., Pinzon, J.E., Brown, M.E., Slayback, D.A., Pak, E.W., Mahoney, R., et al., 2005. An extended AVHRR 8-km NDVI dataset compatible with MODIS and SPOT vegetation NDVI data. Int. J. Remote Sens. 26, 4485–4498.

Verslues, P.E., Agarwal, M., Katiyar-Agarwal, S., Zhu, J., Zhu, J.K., 2006. Methods and concepts in quantifying resistance to drought, salt and freezing, abiotic stresses that affect plant water status. Plant J. 45, 523–539.

Vicente-Serrano, S.M., Beguería, S., López-Moreno, J.I., 2010a. A multiscalar drought index sensitive to global warming: the standardized precipitation evapotranspiration index. J. Clim. 23, 1696–1718.

Vicente-Serrano, S.M., Beguería, S., López-Moreno, J.I., Angulo, M., El Kenawy, A., 2010b. A new global 0.5 gridded dataset (1901–2006) of a multiscalar drought index: comparison with current drought index datasets based on the Palmer Drought Severity Index. J. Hydrometeorol. 11, 1033–1043.

Vicente-Serrano, S.M., Gouveia, C., Camarero, J.J., Beguería, S., Trigo, R., López-Moreno, J.I., et al., 2013. Response of vegetation to drought time-scales across global land biomes. Proc. Natl. Acad. Sci. 110, 52–57.

Wang, D., Hejazi, M., Cai, X., Valocchi, A.J., 2011. Climate change impact on meteorological, agricultural, and hydrological drought in Central Illinois. Water Resour. Res. 47.

Wang, S., Zhang, M., Hughes, C.E., Crawford, J., Wang, G., Chen, F., et al., 2018. Meteoric water lines in arid Central Asia using event-based and monthly data. J. Hydrol. 562, 435–445.

Wang, S., Zhang, Y., Ju, W., Chen, J.M., Cescatti, A., Sardans, J., et al., 2021. Response to comments on "Recent global decline of CO2 fertilization effects on vegetation photosynthesis". Science 373, eabg7484.

Wang, X., Biederman, J.A., Knowles, J.F., Scott, R.L., Turner, A.J., Dannenberg, M.P., et al., 2022. Satellite solar-induced chlorophyll fluorescence and near-infrared reflectance capture complementary aspects of dryland vegetation productivity dynamics. Remote Sens. Environ. 270, 112858.

Wigley, T., Raper, S., 1992. Implications for climate and sea level of revised IPCC emissions scenarios. Nature 357, 293–300.

Wilhite, D.A., 2000. Drought as a Natural Hazard: Concepts and Definitions.

Wilhite, D.A., Svoboda, M.D., Hayes, M.J., 2007. Understanding the complex impacts of drought: a key to enhancing drought mitigation and preparedness. Water Resour. Manag. 21, 763–774.

Wu, T., Lu, Y., Fang, Y., Xin, X., Li, L., Li, W., et al., 2019. The Beijing climate center climate system model (BCC-CSM): the main progress from CMIP5 to CMIP6. Geosci. Model Dev. 12, 1573–1600.

Wu, T., Sang, S., Wang, S., Yang, Y., Li, M., 2020. Remote sensing assessment and spatiotemporal variations analysis of ecological carrying capacity in the Aral Sea basin. Sci. Total Environ. 735, 139562.

Xu, Y., Zhang, X., Hao, Z., Singh, V.P., Hao, F., 2021. Characterization of agricultural drought propagation over China based on bivariate probabilistic quantification. J. Hydrol. 598, 126194.

Yang, J., Chang, J., Wang, Y., Li, Y., Hu, H., Chen, Y., et al., 2018. Comprehensive drought characteristics analysis based on a nonlinear multivariate drought index. J. Hydrol. 557, 651–667.

Yang, Y., Roderick, M.L., Zhang, S., McVicar, T.R., Donohue, R.J., 2019. Hydrologic implications of vegetation response to elevated CO2 in climate projections. Nat. Clim. Chang. 9, 44–48.

Zargar, A., Sadiq, R., Naser, B., Khan, F.I., 2011. A review of drought indices. Environ. Rev. 19, 333–349.

Zhang, G., Su, X., Ayantobo, O.O., Feng, K., 2021. Drought monitoring and evaluation using ESA CCI and GLDAS-Noah soil moisture datasets across China. Theor. Appl. Climatol. 144, 1407–1418.

Zhao, X., Ma, X., Chen, B., Shang, Y., Song, M., 2022. Challenges toward carbon neutrality in China: strategies and countermeasures. Resour. Conserv. Recycl. 176, 105959.